The FASEB Journal

FASEB
Federation of American Societies for Experimental Biology

RESEARCH ARTICLE OPEN ACCESS

Multi-Omics and Machine Learning-Uncovered FLT1-Mediated Epithelial-Endothelial Crosstalk in Cellular Senescence Driving Clear Cell Renal Cell Carcinoma Malignancy

Mouyuan Sun[1,2] | Huchao Mao[1] | Yaxian Luo[2] | Mei Yang[3] | Zhixu He[2] | Shuangyang Li[2] | Zhichao Liu[2] | Lianjie Peng[2] | Quanjie Zhang[1] | Jingyu Zhang[2] | Yan Zhang[1]

[1]Department of Urology, The First Affiliated Hospital of Wenzhou Medical University, Wenzhou, China | [2]Stomatology Hospital, School of Stomatology, Zhejiang University School of Medicine, Zhejiang Provincial Clinical Research Center for Oral Diseases, Zhejiang Key Laboratory of Oral Biomedical, Hangzhou, China | [3]Intensive Care Unit, The First Affiliated Hospital of Wenzhou Medical University, Wenzhou, China

Correspondence: Mouyuan Sun (sunmouyuan777@zju.edu.cn) | Yan Zhang (zhangyan@wmu.edu.cn)

Received: 8 September 2025 | **Revised:** 14 March 2026 | **Accepted:** 2 April 2026

Keywords: cellular senescence | clear cell renal cell carcinoma | epithelial-endothelial interaction | multi-omics | VEGFA/FLT1/AKT1 axis

ABSTRACT

Clear cell renal cell carcinoma (ccRCC) is distinguished by the absence of definitive diagnostic markers and efficacious treatment modalities, factors that collectively contribute to its unfavorable clinical prognosis. The targeting of senescent cells has recently emerged as a promising therapeutic strategy. Nevertheless, the precise role of cellular senescence in the pathophysiology of ccRCC has yet to be comprehensively elucidated. This study sought to investigate the role of cellular senescence levels in ccRCC through comprehensive transcriptomic, proteomic, spatial transcriptomic, and single-cell analyses. The study determined that elevated levels of cellular senescence contribute to a suppressed immune microenvironment, thereby exacerbating the prognosis for ccRCC patients. We utilized an extensive array of machine learning algorithms, in conjunction with multi-omics technologies, validated through immunofluorescence, RT-qPCR, and additional techniques, to collectively identify FLT1 as a pivotal single gene driving ccRCC progression. Our work reveals a FLT1-centered network of related factors, where FLT1 acts as the core single gene, closely associated with key factors VEGFA and AKT1. This network mediates crosstalk between endothelial and epithelial cells: endothelial cells expressing FLT1 alone, AKT1 alone, or co-expressing FLT1/AKT1 exhibited enhanced malignancy; among epithelial cells, proximal tubular epithelial cells with high VEGFA expression (a factor closely related to FLT1) represented the most aggressive subtype and acted as "pioneer cells" driving tumor progression. This FLT1-centric mechanism is evolutionarily conserved, as validated in mouse single-cell datasets. Clinically, ccRCC patients with low expression of the FLT1-centered network (particularly low FLT1) showed better responses to immunotherapy. For patients with high FLT1 expression, a combination therapy targeting this network—screened via molecular docking and dynamics simulations—may improve prognosis. This includes FLT1 inhibitors (Sorafenib, Regorafenib, Lenvatinib), supplemented by AKT1 inhibitors (Capivasertib) and VEGFA inhibitors (Bevacizumab) to suppress FLT1-associated malignant cell populations.

Mouyuan Sun, Huchao Mao, and Yaxian Luo contributed equally to this work.

1 | Introduction

Renal cell carcinoma (RCC) is among the 10 most common malignant tumors worldwide, and approximately 70% of patients are diagnosed with clear cell renal cell carcinoma (ccRCC) [1, 2]. ccRCC is the most common and deadliest subset of renal cancer, with approximately 180000 deaths worldwide each year [3, 4]. Clinically, ccRCC often presents with subtle early symptoms, leading to difficulties in early diagnosis, and as a result, it is frequently detected at advanced stages with metastasis to surrounding tissues or other organs, complicating treatment [5]. Current therapeutic approaches for ccRCC include surgical resection, targeted therapy, and immunotherapy [6, 7]. Advanced ccRCC has spread and metastasized, making it impossible to cure with surgery. Current first-line treatments for advanced ccRCC include angiogenesis inhibitors, mTOR (mammalian target of rapamycin) inhibitors, and immune checkpoint inhibitors [8, 9]. Despite advancements in current treatment modalities, managing ccRCC still faces numerous challenges [10]. For instance, response rates to targeted therapies and immunotherapy are variable, and patients may develop resistance to these treatments [11]. Moreover, the lack of reliable predictive biomarkers limits our ability to forecast treatment outcomes and implement personalized therapies [12, 13]. With deeper insights into cancer biology, particularly regarding the tumor microenvironment and intercellular interactions, our understanding of treatment prospects for advanced cancer patients has improved [14, 15]. These findings highlight the urgency of exploring new therapeutic targets, including the development of novel drugs and the improvement of existing treatment strategies, to achieve more precise personalized therapy.

Cellular senescence is considered one of the hallmarks of cancer, and its role in cancer cells is complex and multifaceted [16, 17]. Some studies indicate that inducing tumor cells into senescent states can effectively inhibit their proliferation and spread, thereby suppressing tumor growth [18, 19]. Senescent cancer cells exhibit heightened immunogenicity, capable of activating dendritic cells (DCs) and specific CD8 T cells to induce anti-tumor immune responses [20]. Nevertheless, other studies indicate that cellular senescence could potentially enhance the malignant traits of tumor cells, including their proliferation, invasiveness, and metastatic capabilities [21, 22]. Additionally, it contributes to the creation of an immunosuppressive tumor microenvironment, a pivotal mechanism for developing drug resistance [23, 24]. Currently, senescence therapies primarily focus on two aspects: inducing tumor cell senescence and selectively eliminating senescent cells [25]. However, the dual nature of senescence complicates the selection of treatment strategies. Therefore, a thorough understanding of the intricate roles of cellular senescence in tumors is essential. This necessitates investigating how tumor cells exploit senescence mechanisms to gain survival advantages and exploring ways to manipulate these processes to design more effective treatment strategies. In-depth studies on the senescence status within ccRCC will help identify critical malignant cell populations driving ccRCC progression. Targeting these malignant cell populations could more effectively control tumor development while minimizing damage to normal cells, thus offering more precise and personalized treatment options for patients.

Tumor heterogeneity poses a complex challenge in cancer therapy, stemming from the diversity of tumor cells and their interactions with the surrounding microenvironment [26]. Multi-omics technologies provide comprehensive insights into tumor cells across different biological levels, aiding in the discovery of novel biomarkers, prediction of patient prognosis, and treatment response [27, 28]. While bulk sequencing captures global information rapidly under specific conditions, it offers a "mean" of cell populations that may mask intercellular heterogeneity [29, 30]. The emergence of single-cell sequencing allows us to observe gene expression patterns at the level of individual cells, revealing the diversity and heterogeneity within cell populations [13, 31, 32]. However, this technique may lead to spatial information loss and damage to fragile cells and tissues during sample processing. Spatial transcriptomics preserves spatial information of gene expression, enabling us to observe spatial heterogeneity during tumor development, crucial for understanding the tumor microenvironment and intercellular interactions [33, 34]. By integrating these data, we can delve deeper into analyzing tumor heterogeneity, elucidating mechanisms underlying tumor initiation and progression. With the rapid development of machine learning technology, new approaches have been developed for processing and analyzing complex and diverse omics data [35, 36]. By applying a combination of various machine learning algorithms, we can accurately identify patterns and rules within data, uncovering hidden biological insights [37, 38]. These discoveries not only deepen our understanding of the biological mechanisms of tumors but also provide more reliable support for biomedical research and clinical diagnostics. Therefore, the integration of omics methods with machine learning has become an important tool in cancer research, offering new perspectives and possibilities for better understanding and addressing the challenges of cancer.

In this study, we have preliminarily confirmed that cellular senescence plays a pivotal role in influencing the clinical prognosis of patients with ccRCC, with an increased level of cellular senescence resulting in a worse clinical prognosis for ccRCC. Based on this finding, we constructed a prognostic signature related to cellular senescence, aiming to predict the clinical outcomes and treatment responses of ccRCC patients. Utilizing a plethora of machine learning algorithms (KNN (K-Nearest Neighbors), Elastic net, GBM (Gradient Boosting Machine), PLS (Partial Least Squares), SVM (Support Vector Machine), Naive Bayes, stepLDA (Stepwise Linear Discriminant Analysis)) and multi-omics technologies (transcriptomics, proteomics, single-cell, and spatial transcriptomics analysis), we identified that a FLT1-centered network of related factors (including VEGFA and AKT1) plays a critical role in the progression of ccRCC mediated by cellular senescence. Our research results indicate that the abnormal activation of this FLT1-centered network of related factors alters the interaction patterns and differentiation potential of endothelial and epithelial cell subpopulations, having a key impact on determining cell fate. Further analysis revealed that within this network, FLT1-positive endothelial cells, AKT1-positive endothelial cells, FLT1- and AKT1-double-positive endothelial cells, and VEGFA-positive epithelial cells (key cell subpopulations associated with the network) exhibit a significant increase in malignancy, and the frequent interactions between these cells are key factors leading to poor prognosis

in ccRCC. Based on drug sensitivity analysis and molecular docking, we have screened several drugs targeting this FLT1-centered network of related factors, including AKT1 inhibitors Capivasertib, VEGFA inhibitors Bevacizumab, as well as FLT1 inhibitors Sorafenib, Regorafenib and Lenvatinib. The discovery of these drugs provides a theoretical basis for a combined targeted treatment strategy, which is expected to accurately target and suppress the malignancy of highly malignant tumor cells. Overall, this study not only deepens our understanding of the mechanisms of cellular senescence in ccRCC but also provides a solid foundation for the development of personalized precision medical strategies.

2 | Materials and Methods

2.1 | Data Collection and Processing

The TCGA-KIRC dataset and clinical data for clear-cell Renal Cell Carcinoma (ccRCC) were obtained from The Cancer Genome Atlas (TCGA) database (https://portal.gdc.cancer.gov/). Seventy-two normal samples and 542 ccRCC samples in total were used in the analysis. R software was used to divide TCGA-KIRC into a training group and a test group at a 3:7 ratio. In addition, two other datasets containing ccRCC tissues and normal tissues were downloaded from the GEO database (https://www.ncbi.nlm.nih.gov/). The GSE105261 dataset contained 35 ccRCC patients' tumor samples and 9 normal tissues, while the GSE168845 dataset contained 4 tumor tissues. The CellAge database (https://genomics.senescence.info/cells/) contains 665 genes relevant to cellular senescence. Cellular senescence pathway genes obtained from KEGG (https://www.kegg.jp/), containing 155 genes (entry: map04218).

2.2 | Identification of the Cellular Senescence-Related Genes

Differential analysis was performed on 542 tumor tissues and 72 normal tissues using the "limma" package to identify DEGs [13, 30]. The heatmap and volcano maps of DEGs were visualized using the "ggplot2" and "pheatmap" packages. Subsequently, the most significant enrichment pathways and biological processes of DEGs were investigated using the GO analysis via the "clusterProfiler" package. In the training set, ccRCC-associated genes were filtered through WGCNA using the "WGCNA" package. Consensus clustering was used to determine the optimal cellular senescence clusters using the "ConsensusClusterPlus" program in order to better uncover the expression patterns of genes linked to cellular senescence in ccRCC. The optimal number of clusters was determined using a consensus matrix and a cumulative distribution function (CDF). The K–M approach was applied to ascertain the variations in survival between clusters. The intersection of DEGs, ccRCC module genes, and cellular senescence-related genes was extracted to construct a cellular senescence-related prognostic signature. To quantify senescence activity at the single-sample level, senescence scores were calculated using the AUCell algorithm. For subsequent stratification and risk grouping, samples were dichotomized into "Senescence-High" and "Senescence-Low" groups using the median senescence score of the cohort as the threshold. This median-based cutoff provides a standard, objective, and reproducible criterion that ensures balanced group sizes for downstream comparative analyses.

2.3 | Construction of Prognostic Signature

To determine if the filtered important genes were negative predictors for cancer prognosis, univariate Cox regression analysis was employed. Least absolute shrinkage and selection operator (LASSO) regression analysis was performed to identify signature genes using the "glmnet" package. The risk score was calculated using the following formula:

$$\text{Risk score} = e^{\sum_{i=1}^{n} \text{Corf}(i)X(i)}.$$

Based on the median risk score, patients with ccRCC were classified into low- and high-risk categories. A prognostic study using K-M survival was performed for individuals with low- and high-risk ccRCC. To verify the stability of the forecast, a ROC curve was created. The R package "pROC" was used to plot the ROC Curve of statistically significant CSRGs and calculate the Area Under the Curve (AUC) value. The AUC of the ROC curve was generally between 0.5 and 1. The closer the AUC is to 1, the better the diagnostic performance. When AUC was between 0.5 and 0.7, the accuracy was low; when AUC was between 0.7 and 0.9, the accuracy was moderate; and when AUC was above 0.9, the accuracy was high.

A nomogram was created based on risk, age, sex, tumor node metastasis classification, and clinical stage in order to further enhance the clinical usefulness. To illustrate the correlation between the actual and predicted probability for the 1, 3, and 5 years of OS, a calibration curve was created. ROC analysis was used to assess each factor's discriminating performance for ccRCC. A principal component analysis (PCA) was performed to assess how well low- and high-risk ccRCC could be separated.

2.4 | Functional Enrichment Analysis

Gene set enrichment analysis (GSEA) was performed to analyze variations in pathway activities between low- and high-risk ccRCC ($p < 0.05$) using GSEA 4.1.0 (http://www.broad.mit.edu/gsea). Gene Ontology (GO) and KEGG analysis were conducted with the DEGs in low- and high-risk ccRCC identified via the "limma" package.

2.5 | Immune Cell Infiltration

In order to investigate the correlation between immune cell infiltration and cellular senescence-related signatures, immune cell infiltration was assessed using the XCELL, TIMER, QUANTISEQ, MCPCOUNTER, EPIC, CIBERSORT-ABS, and CIBERSORT algorithms in different colors. Infiltration scores of 23 types of immune cells, 13 types of immune function-related pathways, and 7 types of stromal-related pathways were calculated by ssGSEA using the "GSVA" package. Furthermore,

the "ESTIMATE" package was utilized to compute three TME-related scores: the immune score, stromal score, and ESTIMATE score.

2.6 | Identification of the Key Signaling Axis Based on Machine Learning

We arranged 101 combinations of these 10 algorithms (Lasso, Ridge, glmBoost, stepglm LDA, random survival forest (RSF), elastic net (Enet), partial least squares regression for Cox (plsRcox), generalized boosted regression modeling (GBM), and support vector machine (SVM)) in the TCGA-KIRC training dataset for variable selection and model construction based on a tenfold cross-validation framework and screened for key genes associated with cellular senescence in ccRCC [39]. Then, we employed seven machine learning algorithms, including KNN (K-Nearest Neighbors), Elastic net, GBM (Gradient Boosting Machine), PLS (Partial Least Squares), SVM (Support Vector Machine), Naive Bayes, and stepLDA (Stepwise Linear Discriminant Analysis), to further screen and identify FLT1, AKT1, and VEGFA as key genes.

2.7 | Single-Cell Analysis of Human Samples

The scRNA-seq dataset GSE156632 was downloaded from the GEO database. RNA-seq data and sample annotation information were processed using the "Seurat" R package. Cells with < 200 genes, > 3500 genes, $> 15\%$ mitochondrial genes, or $> 3\%$ hemoglobin gene content were excluded. After normalizing the scRNA-seq data and modeling the relationship between average expression and dispersion, highly variable genes were identified. To integrate data from multiple samples/batches and mitigate technical variation, we performed batch effect correction using the Harmony algorithm. Specifically, principal component analysis (PCA) was first performed on the integrated dataset. The Harmony function was then applied to these PCA embeddings, using sample origin as the batch covariate, to obtain corrected dimensionality reductions. These Harmony-corrected embeddings were used for subsequent nonlinear dimensionality reduction and clustering. A t-distributed stochastic neighbor embedding (tSNE) plot was generated for visualization and to classify cells into distinct clusters. Differentially expressed genes (DEGs) for each resulting cell cluster were identified using the "FindAllMarkers" function.

To explain the molecular mechanism of ccRCC progression and compare the distinct differentiation patterns between tumor and normal samples, pseudo-time analysis was performed using the "CytoTRACE" algorithm. The CellChat package was employed to analyze cell–cell communication patterns. To avoid confounding signals between tumor and normal tissue, analyses were performed separately on cells derived from tumor samples and those from adjacent normal samples. This approach enabled the identification of dominant senders, receivers, mediators, and influencers within the intercellular communication networks specific to the tumor microenvironment and the normal tissue context, allowing for a comparative assessment of their differences. Each cell's CNV assessment was conducted using the "infercnv" R package. CNVs for epithelial and endothelial cells were calculated separately, with Epi_N and Other serving as references. The parameters for the inferCNV analysis include "denoise," the default Hidden Markov Model (HMM) settings, and a "cutoff value" of 0.1.

2.8 | Single-Cell Analysis of Mouse Samples

The single-cell RNA dataset GSE259361 was downloaded from the GEO database. RNA sequencing data and sample annotation information were obtained through the "Seurat" R package. Cells with fewer than 200 genes, more than 3500 genes, a mitochondrial gene ratio exceeding 15%, or a hemoglobin ratio exceeding 3% were excluded. The single-cell RNA sequencing data were standardized and the relationship between average expression and dispersion was controlled. Then, the highly variable genes of each cell type were determined. The "FindAllMarkers" function was used to identify differentially expressed genes (DEGs) of the given cell type, and tSNE was used for dimensionality reduction processing, classifying the cells into different clusters.

The cellular senescence-related genes were projected in normal samples and tumor samples and presented in a heatmap format. Pseudo-time analysis was performed using the "CytoTRACE" algorithm and the "Monocle" algorithm. The cell communication patterns were analyzed using the CellChat package.

2.9 | Spatial Transcriptomics Analysis

The GSE175540 dataset was downloaded from the GEO database, which contained 24 ccRCC human tumors analyzed by spatial transcriptomics. Spatial transcriptomics data analysis was performed using the "Seurat" R package, employing methods similar to those used for single-cell RNA sequencing data analysis. The "FindTransferAnchors" and "TransferData" functions, with default settings from the "Seurat" R package, were utilized to predict single-cell data on the spatial transcriptomics data.

2.10 | Prediction of Immunotherapy Response

IPS is used to detect the immunogenicity of tumors and predict their response to immunotherapy. Statistical analysis is conducted to estimate the differences in IPS between the high-expression group and the low-expression group of FLT1, AKT1, and VEGFA in order to compare the immunotherapy responses between the two groups.

2.11 | Drug Sensitivity Analysis and Molecular Docking

The drugs were downloaded from ChEMBL database (https://www.ebi.ac.uk/chembl/). Then, the 2D structures of potential active ingredients and key DEG targets were downloaded from PubChem (https://pubchem.ncbi.nlm.nih.gov/) and PDB databases (http://www.rcsb.org/), and were analyzed using the

"AutoDock" package for molecular docking of VEGFA/FLT1/AKT1 axis and small molecule drugs using Lamarckian genetic algorithms (LGA), with all parameters in the genetic algorithm at default values.

2.12 | Molecular Dynamics Simulations

Gromacs2022.3 software was used for molecular dynamics simulation [40, 41]. For small molecule preprocessing, AmberTools22 is used to add GAFF force field to small molecules, while Gaussian 16 W is used to hydrogenate small molecules and calculate RESP potential. Potential data will be added to the topology file of the molecular dynamics system. The simulation conditions were carried out at a static temperature of 300 K and atmospheric pressure (1 Bar). Amber99sb-ildn was used as the force field, water molecules were used as solvent (Tip3p water model), and the total charge of the simulation system was neutralized by adding an appropriate number of Na + ions. The simulation system adopts the steepest descent method to minimize the energy, and then carries out the isothermal isovolumic ensemble (NVT) equilibrium and isothermal isobaric ensemble (NPT) equilibrium for 100 000 steps, respectively, with the coupling constant of 0.1 ps and the duration of 100 ps. Finally, the free molecular dynamics simulation was performed. The process consisted of 5 000 000 steps, the step length was 2 fs, and the total duration was 100 ns. After the simulation was completed, the built-in tool of the software was used to analyze the trajectory, and the root-mean-square variance (RMSD), root-mean-square fluctuation (RMSF), and protein rotation radius of each amino acid trajectory were calculated, combined with the free energy (MMGBSA), free energy topography, and other data.

2.13 | Protein Expression and Subcellular Localization

We utilized the Human Protein Atlas database (HPA) (website: https://www.proteinatlas.org) to analyze the immunohistochemical staining images of FLT1, VEGFA, and AKT1 in ccRCC and normal tissues, as well as the subcellular localization of FLT1.

2.14 | Real-Time Quantitative Polymerase Chain Reaction (RT-qPCR) Analysis

Total RNA from tumor tissues and normal control tissues was extracted using TRIzol reagent (Invitrogen, USA). First-strand cDNA was synthesized using a Superscript II First-Strand cDNA Synthesis Kit (TaKaRa, Japan). GAPDH was used as an internal control.

2.15 | Cell Culture

The human clear cell renal cell adenocarcinoma cell line (786-O) was cultured in RPMI-1640 medium supplemented with 10% fetal bovine serum (ZETA, USA) and 1% penicillin–streptomycin solution (Gibco, USA) at 37°C in a 5% CO_2 incubator. Human umbilical vein endothelial cells (HUVECs) were cultured in endothelial cell medium, supplemented with 5% fetal bovine serum, 1% endothelial cell growth supplement, and 1% penicillin–streptomycin solution, and maintained at 37°C in a 5% CO_2 incubator.

For the co-culture experiments, HUVECs were seeded in the lower chamber of a Transwell plate, while epithelial cells were plated in the upper chamber. After cell attachment, the medium in the upper chamber was replaced with fresh medium containing recombinant human VEGFA (MCE, Cat# HY-P7110A) or vehicle control, and the co-culture was continued for 24 h. Subsequently, endothelial cells from the lower chamber were harvested for RNA extraction and RT-qPCR analysis.

2.16 | Immunofluorescence

We blocked paraffin sections with BSA and then incubated them with primary antibodies (anti-FLT1, anti-AKT1, anti-CD34, anti-VEGFA, anti-KRT8) overnight at 4°C in a humidified chamber. Slides were then incubated with fluorescein-conjugated secondary antibodies for 1 h at room temperature in the dark. Nuclei were counterstained with 4′, 6-diamidino-2-phenylindole (DAPI) [42]. We used confocal microscopy (Nikon) for imaging. Antibody catalog number: anti-FLT1 (Proteintech, Wuhan, China, 13687-1-AP), anti-AKT1 (Abcam, Cambridge, UK, ab235958), anti-CD34 (Abcam, Cambridge, UK, ab81289), anti-VEGFA (Proteintech, Wuhan, China, 19003-1-AP), anti-KRT8 (Proteintech, Wuhan, China, 27105-1-AP).

2.17 | FLT1 Knockdown

786-O cells were transfected with FLT1-specific siRNA (Sense: 5′-GCCCAUCACUAUGGAAGAUTT-3′; Antisense: 5′-AUCUUCCAUAGUGAUGGGCTT-3′, Genema, China) following the manufacturer's protocol for gene silencing. Transfection efficiency was validated by RT-qPCR analysis 24 h post-transfection.

2.18 | Wound Healing Assay

786-O cells were seeded at a density of 2×10^4 cells/mL in 6-well plates and cultured in RPMI-1640 with serum-free medium. Parallel scratches (approximately 1 mm wide) were created on the cell monolayer using a sterile 200 μL pipette tip perpendicular to the plate bottom. Images of the scratched areas were captured at 0 h (immediately after scratching) and 24 h using a microscope, and the wound width was measured using ImageJ software.

2.19 | Live/Dead Staining

786-O cells were plated in 12-well plates and treated with FLT1-specific siRNA for 24 h. Live/dead staining was performed using a mixture of PBS, calcein-AM, and propidium iodide (KeyGEN BioTECH, China). The mixture was introduced directly to the wells and cultured at 37°C for 30 min.

2.20 | Cytotoxicity Assay

For cell proliferation assessment, 786-O cells were plated in 96-well plates and treated with FLT1-specific siRNA for 24 h. Cell viability was evaluated using a Cell Counting Kit-8 (CCK-8, GLPBIO, USA). The CCK-8 solution was diluted 1:10 with medium and added to the cells, followed by incubation at 37°C for 1 h. Subsequently, the supernatant from each well was collected, and the optical density (OD) was measured at 450 nm.

2.21 | Statistical Analysis

Statistical analysis and graphs were generated using R software V4.0.2 and GraphPad Prism 10.0. While comparing continuous variables between two groups, the Student's *t*-test or Wilcoxon rank-sum test was utilized; while comparing the differences between three groups, one-way ANOVA or Kruskal–Wallis tests were employed. Pearson's correlation was used to calculate correlations between regularly distributed data, while Spearman's correlation was used to evaluate correlations between non-normally distributed variables. The cutoff point for statistical significance was $p < 0.05$.

3 | Results

3.1 | Importance of Cellular Senescence Involvement in ccRCC Occurrence and Development

By applying single-cell analysis technology, we are able to delve into the specific characteristics exhibited by different cell populations during the process of cellular senescence. After quality control and clustering, we obtained core cells for subsequent analysis (Figure S1A–N). Marker genes were used to annotate cell types, and based on the expression levels of these genes, the core cells were classified into five independent cell clusters, including immune cells, fibroblasts, epithelial cells, and endothelial cells (Figure 1A–D). GO and KEGG analysis showed that the marker genes in ccRCC tissue were enriched in various pathways related to tumor progression, such as cell chemotaxis, tissue migration, and focal adhesion (Figures 1D and S1O–R). Compared to normal tissues, ccRCC tissues had a decreased percentage of epithelial cells and an increased percentage of endothelial and immune cells (Figure 1E). Further, we evaluated the cellular senescence level of various cell types using the "AUcell" algorithm. The analysis showed that cellular senescence was generally increased in ccRCC tissues (Figure 1F). We then selected several key genes involved in cellular senescence and employed the "tSNE" algorithm to project them. This revealed that the majority of these genes exhibited differential expression and distribution patterns in normal and ccRCC tissues (Figure 1G). Furthermore, transcriptome analysis was employed to substantiate this finding that the level of cellular senescence is markedly elevated in ccRCC tissues (Figure 1H,I). Patients exhibiting elevated cellular senescence levels were confirmed to have a poorer clinical prognosis in multiple clinical cohorts (Figure 1J). These results suggest that cellular senescence may be a mechanism that plays a pivotal role in the progression of ccRCC. However, the precise mechanism remains to be elucidated.

3.2 | Identification of Key Cell Senescence-Related Genes in ccRCC

Cellular senescence-related genes were obtained from the CellAge database. We conducted an unsupervised consensus analysis with the objective of elucidating the molecular heterogeneity of ccRCC from the perspective of cellular senescence-related genes. The results indicated that $k = 2$ was more reasonable, with all samples divided into two ccRCC subtypes (C1 subtype and C2 subtype) (Figure S2A–D). The C2 subtype exhibited a lower level of cellular senescence than the C1 subtype (Figure 2A). We conducted a Kaplan–Meier survival analysis to assess the correlation between the two ccRCC subtypes and clinical outcomes. The results demonstrated that the C2 subtype exhibited a significantly longer overall survival than the C1 subtype ($p = 0.0165$) (Figure 2B). We subjected the differentially expressed genes (DEGs) between the C1 and C2 subtypes to GSEA enrichment analysis, which demonstrated that these genes were predominantly associated with the endoplasmic reticulum lumen, epidermis development, epithelial cell differentiation, natural killer cell-mediated immunity, response to wounding, and antimicrobial humoral immune response mediated by antimicrobial peptide. This suggests that cellular senescence may be closely related to cellular development and the immune microenvironment (Figure 2C). Consequently, we proceeded to investigate the relationship between cellular senescence and the immune microenvironment. The findings revealed a positive correlation between cellular senescence and immune pathways, including parainflammation, MHC_classI, C-C Motif Chemokine Receptor (CCR), checkpoint, and others. Additionally, a positive correlation was observed between cellular senescence and various immune cells. Regulatory T cells (Treg cells), acting as immunosuppressive cells, are closely positively correlated with the level of cellular senescence. As the level of cellular senescence increases, more Treg cells in the tumor microenvironment are activated, which may lead to an immunosuppressive environment, resulting in poorer prognosis and reduced therapeutic efficacy in ccRCC (Figure 2E).

To further investigate the potential relationship between the DEGs between the normal and ccRCC tissues and cellular senescence, a differential analysis was conducted to identify significant DEGs (Figure 2F,G). GO and KEGG analysis results indicated that the DEGs were predominantly enriched in pathways related to the regulation of epithelial cells, the regulation of endothelial cells, and angiogenesis. These findings suggest that the abnormal cellular behavior of epithelial and endothelial cells, along with increased angiogenesis, may be key mechanisms contributing to the progression of ccRCC (Figure 2H). To identify genes involved in ccRCC occurrence and development, we employed weighted correlation network analysis (WGCNA) (Figures 2I and S2E–G). Based on the correlation coefficient and P-value, the magenta module was identified as the key module (Figure 2J). Figure 2K illustrates the protein–protein interactions

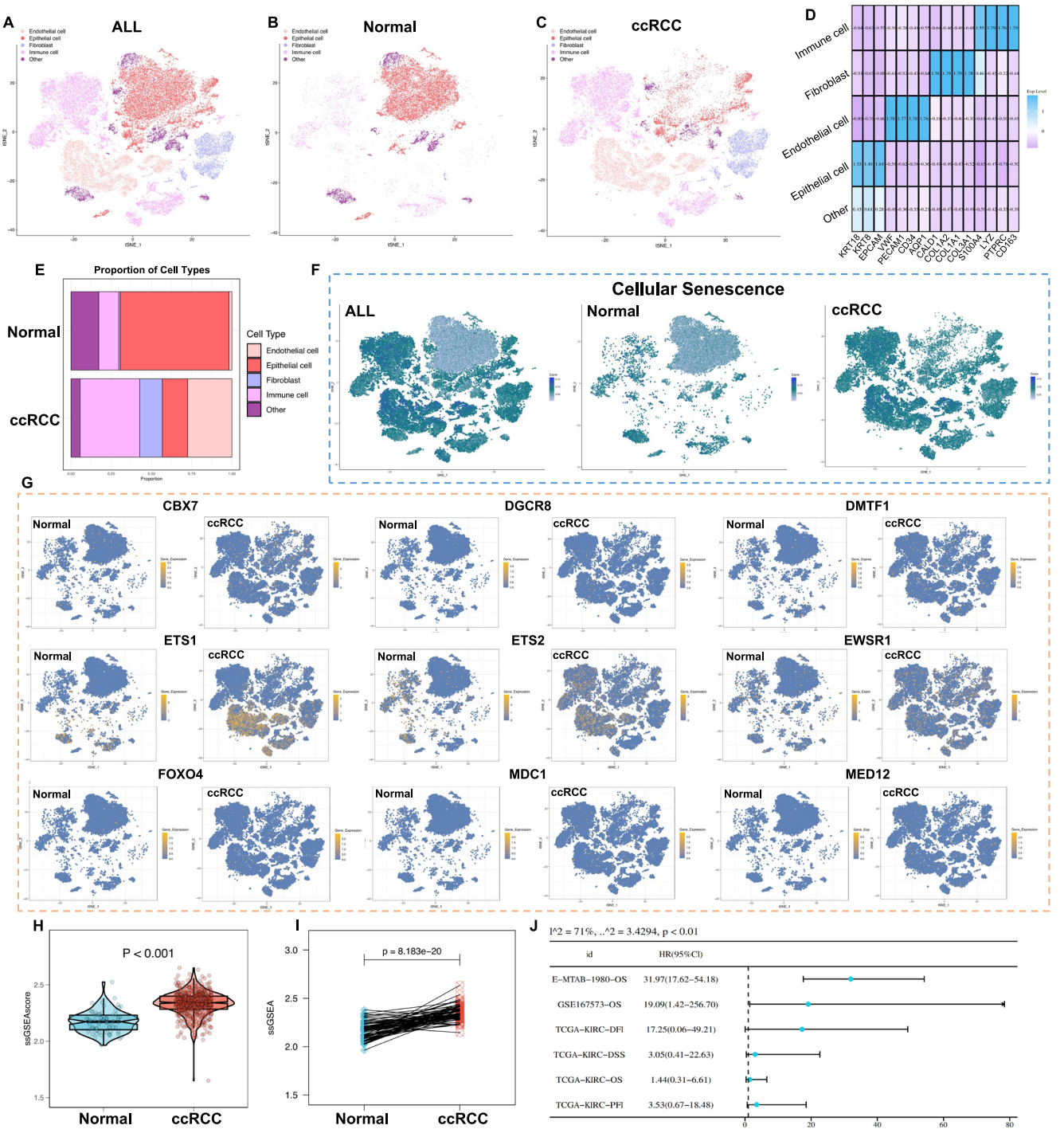

FIGURE 1 | Importance of cellular senescence involvement in ccRCC. (A–C) tSNE representation of major cell types identified by scRNA-seq. (D) Marker genes expressed in 5 major cell types. (E) Bar graph of relative cell proportions. (F) Cellular senescence level of various cell types using the "AUcell" algorithm. (G) Expression of cellular senescence-related genes is shown in tSNE. (H) Different ssGSEA score of cellular senescence between the Normal and ccRCC groups. (I) Different ssGSEA score of cellular senescence between the Normal and ccRCC groups based on paired samples. (J) Meta-analysis of cellular senescence score and prognosis in multiple clinical cohorts of patients.

between the genes in the magenta module. The intersection between cellular senescence-related genes, key WGCNA module genes, and DEGs between ccRCC and normal tissues was demonstrated using Venn diagrams. Subsequently, 154 intersecting genes were identified as key cellular senescence-related genes associated with ccRCC occurrence and development, and were subjected to further analysis (Figure 2L).

3.3 | Immune Infiltration Analysis and Tumor Mutational Burden (TMB) Analysis of the Cellular Senescence-Related Prognostic Signature

Through univariate Cox regression analysis of patients with ccRCC, we identified two protective genes (ANLN and

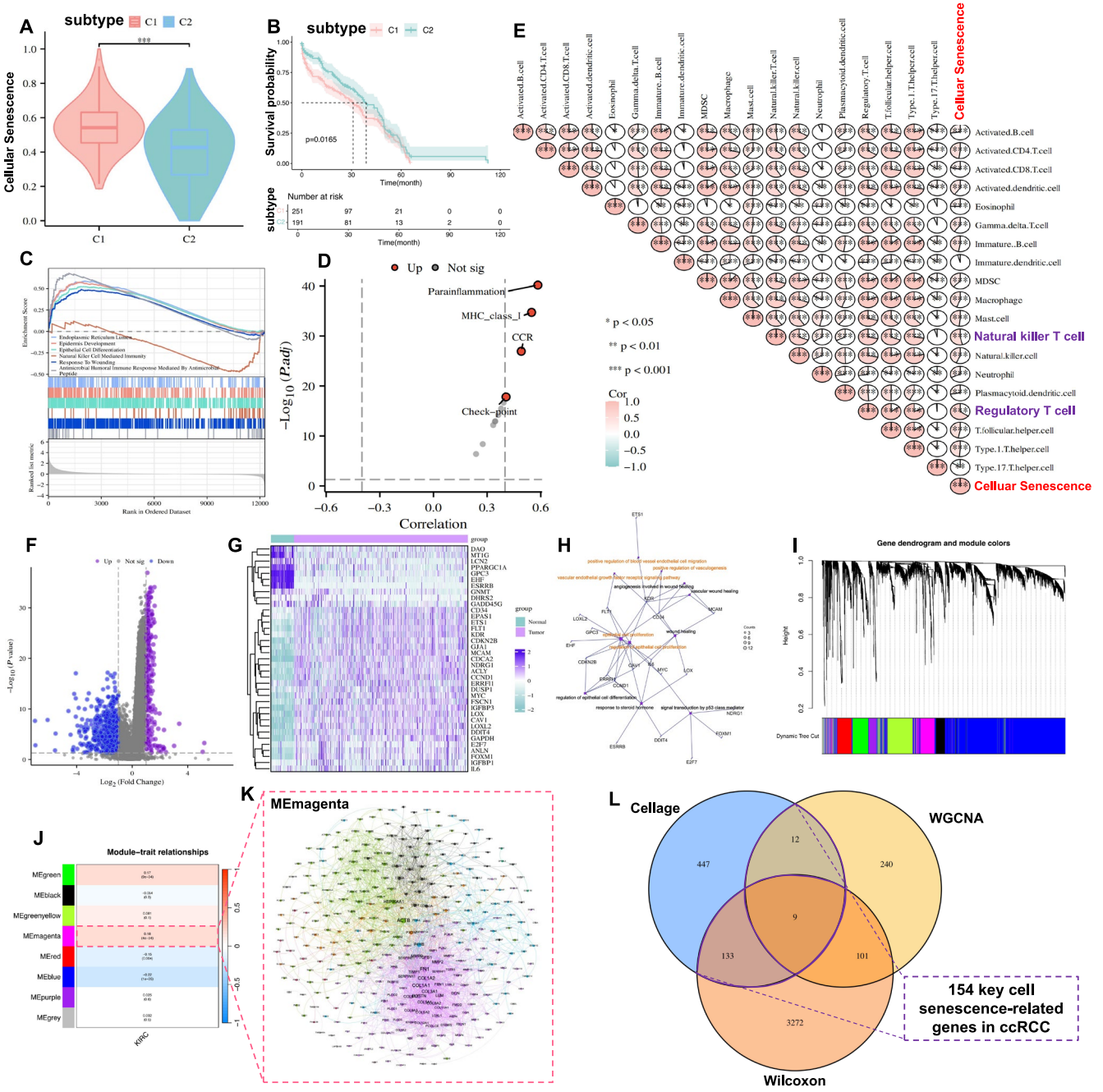

FIGURE 2 | Identification of key cell senescence-related genes in ccRCC. (A) Different cellular senescence scores between C1 and C2 groups. (B) Kaplan–Meier Curves for differential survival of 2 cellular senescence clusters. (C) The top six most significant pathways by GSEA between C1 and C2 groups. (D) Correlation analysis between immune infiltration scores and cellular senescence scores. (E) Correlation analysis between immune cells and cellular senescence scores. (F) Volcano plot of DEGs in the normal and ccRCC groups. (G) Heat map of DEGs in normal and ccRCC groups. (H) GO and KEGG enrichment analysis of the DEGs. (I) Cluster dendrogram of the co-expression network modules. (J) Analysis of correlations between the modules and ccRCC. (K) Protein–protein interaction networks (PPI) in MEmagenta module. (L) Intersection of genes from "Cellage" database, genes in MEmagenta module, and DEGs in ccRCC and normal groups. ***$p < 0.01$.

FOXM1) and five risk genes (CD34, FLT1, GADD45G, GNMT, and NDRG1) (Figure 3A). A prognostic signature constructed using the LASSO algorithm categorized patients into low-risk and high-risk groups, with the latter showing higher mortality rates and upregulated expression of risk genes (Figures 3B and S3A,E,J). K-M survival analysis indicated significantly lower overall survival rates for the high-risk group (Figure S3B,F,J). The ROC curves that vary with time showed AUC values of the three subsets at 1, 3, and 5 years were all greater than 0.60 (Figure S3C,G,K). PCA further confirmed distinct differences between high-risk and low-risk groups (Figure S3D,H,L). Additionally, there were significant differences in N stage, T stage, and clinical staging between the high and low-risk groups (Figure S4A–F). Multivariate Cox analysis revealed that M stage and risk score are independent prognostic indicators (Figure S4G,H). A heatmap of the clinical features and

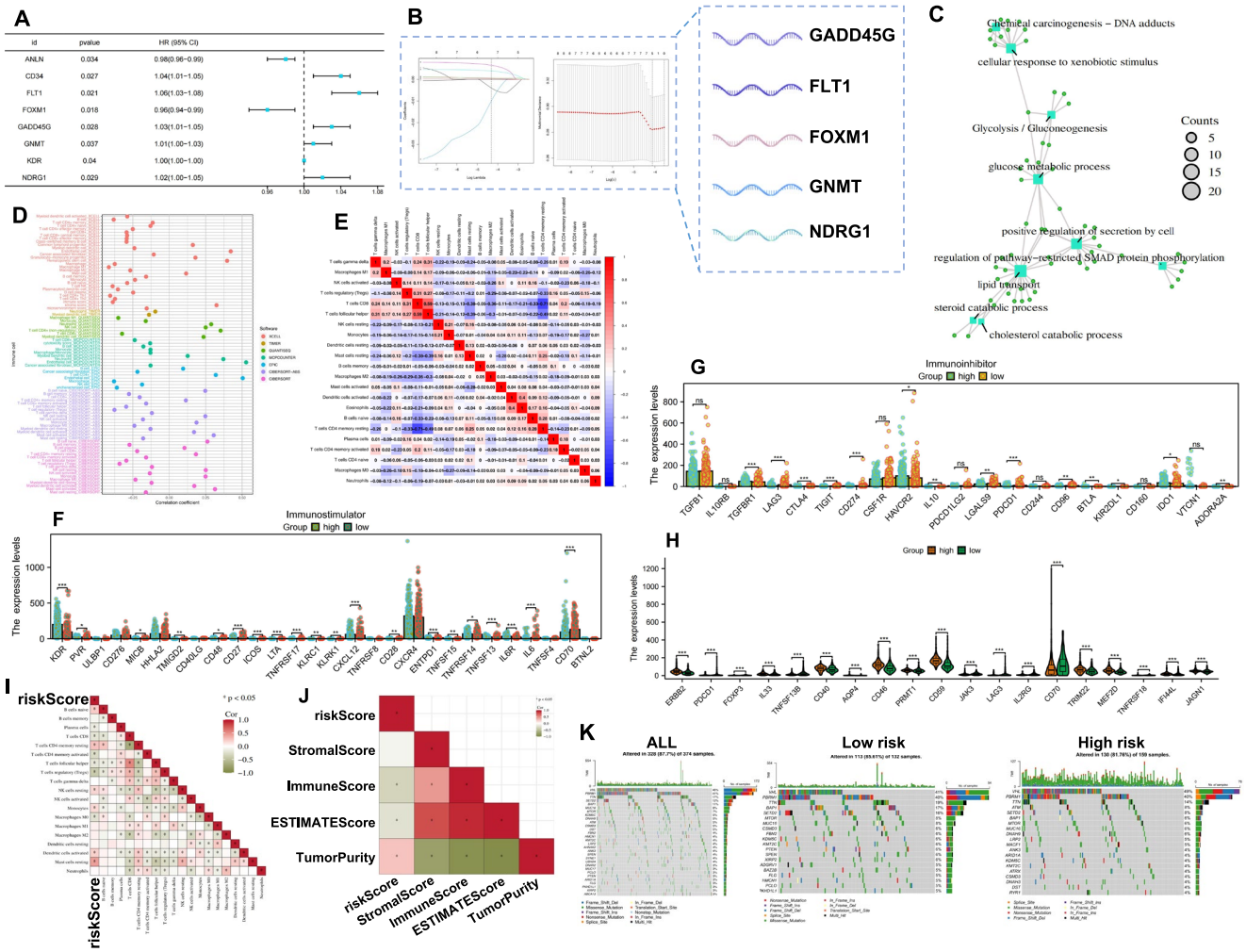

FIGURE 3 | Construction and validation of the cellular senescence-related signature. (A) Univariate Cox analysis of the key genes screened. (B) The cellular senescence-related signature obtained five prognostic genes using LASSO analysis. (C) GO and KEGG enrichment analysis of the DEGs in high- and low-risk groups. (D) Correlation analysis of risk score and diverse immune cells using the XCELL, TIMER, QUANTISEQ, MCPCOUNTER, EPIC, CIBERSORT-ABS, and CIBERSORT algorithms. (E) Correlation analysis of immune cells. (F) Different expression levels of immunostimulator between high- and low-risk groups. (G) Different expression levels of immunoinhibitor between high- and low-risk groups. (H) Different expression levels of humoral immunity-related genes between high- and low-risk groups. (I) Correlation analysis of risk score and immune cells. (J) Correlation analysis of risk score, stromal score, immune score, estimate score and tumor purity. (K) The tumor mutational burden (TMB) analysis. $*p < 0.05$, $**p < 0.01$, and $***p < 0.001$.

cellular senescence-related gene expression levels of the TCGA subset also confirmed this finding (Figure S4I). A nomogram based on M stage and risk score predicted 1-, 3-, and 5-year survival rates for patients, with calibration curves showing good predictive accuracy. ROC analysis indicated that the nomogram has a higher AUC value, making it an effective predictive tool (Figure S4J–L). K-M survival analysis further confirmed that the prognosis of low-risk ccRCC patients is significantly better than that of high-risk patients, especially among those over 65 years old, in stages III-IV, and at T3 stage (Figure S5). These results suggest that cell senescence-related prognostic features are valuable for predicting the clinical outcomes of ccRCC patients.

The enrichment analysis for the high-risk and low-risk groups indicated that the risk score is mainly associated with pathways such as cellular response to xenobiotic stimulus, glycolysis/gluconeogenesis, glucose metabolic processes, positive regulation of secretion by cell, lipid transport, and regulation of pathway-restricted SMAD protein phosphorylation (Figure 3C). These pathways may be the underlying mechanisms that lead to different prognoses for patients in the high-risk and low-risk groups. By combining seven types of immune infiltration algorithms, we found that the risk score was significantly positively correlated with endothelial cells, suggesting that there may be more activated endothelial cells in the tumor microenvironment of high-risk patients, and endothelial cells may be a key cell group leading to poor prognosis in ccRCC (Figure 3D). Figure 3E shows the complex immune microenvironment in ccRCC, where these immune cells interacted with each other. The risk score was closely related to a variety of immune cells, among which, it was positively correlated with various resting state cells, such as T cells CD4 memory resting, NK cells memory, Mast cells resting, and negatively correlated with various immune cells that play anti-tumor immune functions, such as T cells CD8, T cells CD4 memory activated, T cells follicular helper. The

state of Tregs, closely related to immune escape, also changed. These results indicated that the high-risk patients may be in an immunosuppressive state (Figure 3I). In addition, there were differences in the expression levels of multiple immune-inhibitory, immune-stimulatory, and humoral immune genes between the high-risk and low-risk groups (Figure 3F–H). These differences in immune infiltration between the groups may be the basis for different clinical outcomes and responses to immunotherapy. The risk score was negatively correlated with the immune score and the estimation score, while positively correlated with tumor purity (Figure 3J). The TMB of low-risk patients is higher than that of high-risk patients. The above results collectively suggest that low-risk patients may have a better response to immunotherapy. High-risk patients may have lower effectiveness of immunotherapy and are more likely to exhibit immunosuppression (Figures 3K and S3M–O). Therefore, it is necessary for us to identify new targets to treat high-risk populations more effectively.

3.4 | Combining Machine Learning and Experimental Methods to Screen the Most Critical Gene FLT1

To explore more valuable clinical treatment targets to help high-risk patients better overcome their predicament, we further screened key targets among the genes in the prognostic signature construction. We fitted 101 combinatory machine learning methods. A training set and an internal validation set were separated from the TCGA-KIRC dataset at a ratio of 7:3, and the C-index for each model was calculated (Figure 4A). Using a machine learning algorithm, four cellular senescence-related genes with the highest association with ccRCC were screened: FLT1, FOXM1, GGAD45G, and NDRG1 (Figure 4B). In addition, we employed seven machine learning algorithms—KNN, Elastic net, GBM, PLS, SVM, Naive Bayes, and stepwise LDA—to identify the most critical genes in ccRCC. The results showed that three of the machine learning algorithms ranked FLT1 as the most important, while in the other four, the importance of FLT1 was also within the top three (Figures 4C–E and S6). Therefore, combining these results with others, we further identified key genes. The RT-qPCR results showed that among the five mRNAs, only FLT1, GADD45G, and GNMT were highly expressed in ccRCC tissues. Among them, FLT1 is the most significant gene between ccRCC and normal tissues, with its expression in ccRCC tissues being approximately seven times that of normal tissues, higher than the other genes. Therefore, FLT1 is a more reliable therapeutic target (Figure 4F). Clinical cohorts from the GEO database also confirmed the increased expression of FLT1 in ccRCC tissues (Figure S8A).

Single-cell projections demonstrated that FLT1 was predominantly expressed in immune and other cell populations in normal tissues, with a notable increase in expression observed in ccRCC tissues, particularly in endothelial cell populations (Figure 4G–I). In our previous results, we confirmed that endothelial cells are a key cellular population contributing to poor prognosis in ccRCC, which further underscores the significant potential of highly expressed FLT1 in ccRCC endothelial cells as a therapeutic target. According to the CPTAC database, FLT1's mRNA and protein expression were greater in ccRCC tissues than in normal tissues (Figure 4J,K). The subcellular localization of FLT1 to the plasma membrane and the actin filaments was observed (Figure 4L,M). The expression levels of FLT1 in the tissue samples were examined by immunohistochemistry. Consistent with the expectations, FLT1 was highly expressed in ccRCC samples (Figure 4N). Compared to the other four genes, ccRCC patients classified based on the expression levels of FLT1 exhibit more distinct immunological characteristics (Figures S7A and S8B–M). FLT1 was associated with a variety of immune cells, such as pDC, NK cells, and Memory T cells (Figure S7B). GESA revealed that the expression of FLT1 is significantly enriched in immune processes, such as T cell differentiation, NK cell-mediated cytotoxicity, and antibody production involved in immune responses (Figure S7C). Therefore, we believe that FLT1 is not only a reliable therapeutic target, but the level of its expression may also affect the immune microenvironment and consequently alter the response to immunotherapy, which requires further investigation.

To validate the role of FLT1 in the malignant behavior of tumor cells, we used siRNA-mediated gene silencing to effectively inhibit FLT1 expression in 786-O cells (Figure 4O). A wound-healing assay was employed to examine the potential role of FLT1 in cell migration, and it was observed that the migration ability of 786-O cells with disrupted FLT1 expression was significantly suppressed after 24 h (Figure 4P). Through live-dead staining, it was visually observed that the 786-O cells with FLT1 expression interference showed less green fluorescence staining, which was associated with fewer number of live cells (Figure 4Q). Through CCK-8 assays, it was found that interfering with FLT1 expression inhibited the proliferative capacity of 786-O cells (Figure 4R). Furthermore, the levels of the invasion-associated marker VTM were markedly reduced in FLT1-silenced 786-O cells, as determined by RT-qPCR (Figure 4S). Furthermore, to assess the impact of FLT1 on cellular senescence, we examined the expression of key senescence-associated markers. RT-qPCR analysis revealed that FLT1 knockdown led to a significant downregulation of canonical senescence-related genes, including the cyclin-dependent kinase inhibitors CDKN1A (p21) and CDKN2A (p16), as well as several senescence-associated secretory phenotype (SASP) factors (Figure 4T). Together, these findings indicate that FLT1 inhibition attenuates the migratory, proliferative, and survival capacities of ccRCC cells, suppresses the expression of key senescence-associated genes, and thereby contributes to malignant progression, highlighting its potential as a promising therapeutic target.

3.5 | Functional Analysis of FLT1 Based on scRNA-Seq Analysis

Several analyses were conducted to determine the specific mechanism by which FLT1 plays a role in ccRCC progression. Cell–cell communication networks were constructed to predict intercellular communication based on specific pathways and ligand receptors. It is worth noting that, compared with normal tissues, in tumor tissues, the endothelial cells and epithelial cells begin to exhibit significant interactions in terms of both count

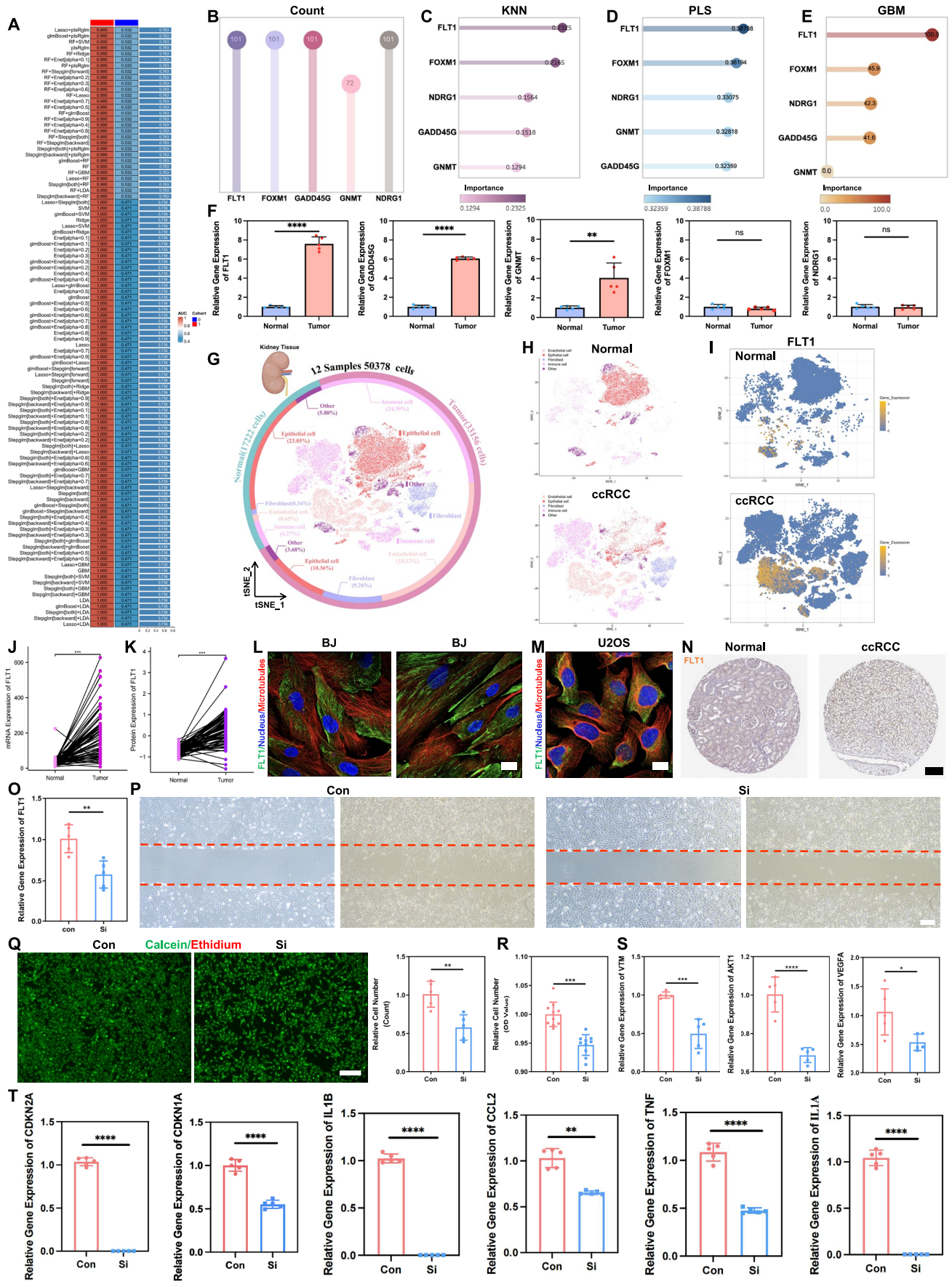

FIGURE 4 | Legend on next page.

FIGURE 4 | Combining machine learning and experimental methods to screen the key gene FLT1. (A, B) Multiple machine learning algorithms showing the importance of five genes in ccRCC. (C) KNN algorithm for the importance of the five genes. (D) PLS algorithm for the importance of the five genes. (E) GBM algorithm for the importance of the five genes. (F) RT-qPCR verifying the expression difference of five genes in tumor and normal groups. (G, H) tSNE classified different cell types and showed the distribution of the types in normal and tumor tissues. (I) Expression of FLT1 in different cell clusters. (J) The mRNA expression of FLT1 in normal and ccRCC tissues based on the CPTAC database. (K) The protein expression of FLT1 in normal and ccRCC tissues based on the CPTAC database. (L) Subcellular localization of FLT1 in BJ cells from HPA datasets. Scale bar = 20 μm. Green: Target protein; Blue: Nucleus; Red: Microtubules. (M) Subcellular localization of FLT1 in U2OS cells from HPA datasets. Scale bar = 20 μm. Green: Target protein; Blue: Nucleus; Red: Microtubules. (N) Available pathology images of FLT1 localization and expression in normal and ccRCC were obtained from the HPA database. Scale bar = 200 μm. (O) The relative expression levels of FLT1 in 786-O cells with FLT1 knockdown. (P) Wound healing in 786-O cells with FLT1 knockdown. Scale bar = 200 μm. (Q) Live/dead staining in 786-O cells with FLT1 knockdown. Scale bar = 200 μm. (R) CCK-8 assay of 786-O cells with FLT1 knockdown. (S) The relative expression levels of VTM, AKT1 and VEGFA in 786-O cells with FLT1 knockdown. (T) The relative expression levels of senescence-associated genes in 786-O cells with FLT1 knockdown. $^{*}p < 0.05$, $^{**}p < 0.01$, $^{***}p < 0.001$, and $^{****}p < 0.0001$.

and weights. In addition, the interactions between endothelial cells and other cell populations were transformed in the tumor state, and the endothelial cells, which mainly acted as senders in the normal state, became the most important receivers in the tumor state and were widely influenced by other cell populations (Figure 5A–C,F–H). In normal tissues, MIF and SPP1 were among the most important signaling pathways through which endothelial cells mainly acted on fibroblasts and immune cells (Figure 5D,E).

However, in tumor tissues, MIF and VEGF were the two most important signaling pathways, with epithelial cells mainly acting as outputs and endothelial cells as inputs. Within the tumor microenvironment, the MIF signaling pathway primarily modulated the interactions between immune cells and epithelial cells, while the VEGF signaling pathway predominantly governs the crosstalk between endothelial cells and epithelial cells (Figure 5I,J). To delve deeper into the specific regulatory mechanisms of FLT1 in ccRCC, we focused our subsequent analysis on the VEGF signaling pathway, which is chiefly involved in the behavior of endothelial cells. VEGF predominantly exerted its effects among endothelial cells, epithelial cells, fibroblasts, and other cell types. Endothelial cells acted as both recipients and influencers, whereas epithelial cells function as initiators. The VEGFA-VEGFR1 (FLT1) receptor-ligand pair was the most critical interaction within this pathway (Figure 5J). Within the VEGF pathway, VEGFR1 (FLT1) had three upstream genes, including VEGFA, VEGFB, and PGF. Utilizing seven machine learning algorithms (including KNN, Naive Bayes, PLS, stepLDA, SVM, Elastic Net, and GBM), we further compared the importance of these three upstream genes, where six out of the seven machine learning algorithms confirmed that VEGFA is the most critical gene, which is consistent with the results of the CellChat analysis (Figures 5K–Q and S9A). The RT-qPCR results indicated that VEGFA and VEGFB were upregulated in ccRCC tissues, while the expression of PGF shows no difference. Among them, the difference in expression levels of VEGFA between normal tissues and ccRCC tissues was the most significant, making it potentially a better choice for a therapeutic target compared to VEGFB and PGF (Figure S11). Both mRNA and protein expression levels of VEGFA indicated its upregulation in ccRCC, which was also corroborated by immunohistochemical results (Figure 5R–T). Therefore, we believe that the VEGFA-VEGFR1 (FLT1) receptor-ligand pair is the most important receptor-ligand pair between endothelial cells and other cells, exerting a key impact on endothelial cell function.

3.6 | Identification of a FLT1-Centered Regulatory Network Associated With Cellular Senescence in ccRCC Through Integrative Machine Learning and Multi-Omics Analysis

Using WGCNA, we filtered key modules associated with cellular senescence and extracted the module in which FLT1 is located. We then performed a protein–protein interaction (PPI) network analysis on the genes within this module, identifying a subset of genes closely related to cellular senescence in the context of FLT1 (Figure 6A,B). Further exploration in the STRING database for genes closely related to FLT1 yielded 34 candidate genes. By intersecting these genes with those in the cellular senescence pathway, we identified two genes, AKT1 and NFATC2, that are intimately associated with FLT1 and involved in cellular senescence (Figure 6C). Correlation analysis revealed a stronger association between AKT1 and FLT1 (Figure 6D). Compared to NFATC2, AKT1 showed a more significant difference across various clinical stages of ccRCC (Figure 6E). Additionally, we applied seven machine learning algorithms (KNN, Naive Bayes, PLS, stepLDA, SVM, Elastic Net, and GBM) to compare the importance of two genes, among which four confirmed that AKT1 is more critical in ccRCC (Figures 6F and S9B–D). Consequently, we focused on AKT1 as a key factor closely associated with FLT1 and propose that a FLT1-centered regulatory network, potentially involving AKT1, plays a significant role in ccRCC-associated senescence. The immunohistochemical results also confirmed that AKT1 exhibited a higher expression in ccRcc compared to normal tissues (Figure 6G).

Transcriptomic analysis revealed that FLT1 and its associated gene AKT1/VEGFA were co-upregulated in ccRCC compared to normal tissues (Figure 6H). Consistent with a functional link, knockdown of FLT1 in 786-O cells led to significant downregulation of AKT1/VEGFA expression (Figure 4V). The expression levels of FLT1, AKT1, and VEGFA were also correlated with immune cell infiltration patterns in ccRCC (Figure 6I). Enrichment and correlation analyses indicated that FLT1 and its associated network are closely related to pathways involved in renal cell carcinoma, cellular

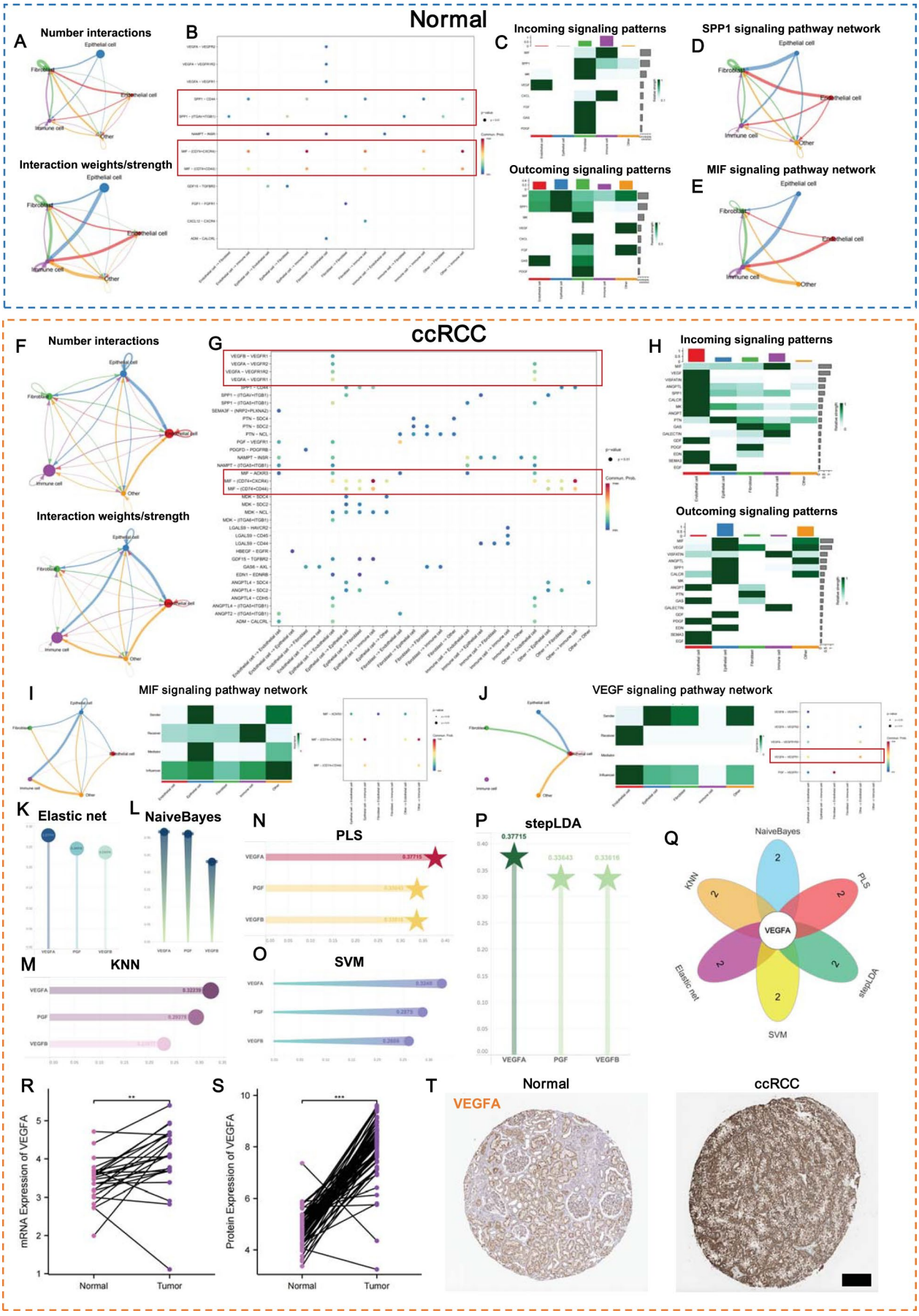

FIGURE 5 | Legend on next page.

FIGURE 5 | Functional analysis of FLT1 based on scRNA-seq analysis. (A) Number and strength of interactions between each cell type in normal tissues. (B) Relative contribution of each ligand-receptor pair to the main signaling pathway network between each cell type in normal tissues. (C) Outgoing and incoming signaling patterns of different cell types in normal tissues. (D) The inferred SPP1 signaling pathway networks in normal tissues. (E) The inferred MIF signaling pathway networks in normal tissues. (F) Number and strength of interactions between each cell type in tumor tissues. (G) Relative contribution of each ligand-receptor pair to the main signaling pathway network between each cell type in tumor tissues. (H) Outgoing and incoming signaling patterns of different cell types in normal tissues. (I) The inferred MIF signaling pathway networks and the heatmap showing the relative importance of each cell group based on the computed four network centrality measures of MIF signaling pathway. The relative contribution of each ligand-receptor pair to the MIF signaling pathway is also shown. (J) Similar to figure L, describing the VEGF signaling pathway. (K) Elastic net identified the most critical upstream genes of FLT1 (VEGFR1). (L) Naive Bayes identified the most critical upstream genes of FLT1 (VEGFR1). (M) KNN identified the most critical upstream genes of FLT1 (VEGFR1). (N) PLS identified the most critical upstream genes of FLT1 (VEGFR1). (O) SVM identified the most critical upstream genes of FLT1 (VEGFR1). (P) StepLDA identified the most critical upstream genes of FLT1 (VEGFR1). (Q) Venn diagrams showed the most critical upstream genes of FLT1 (VEGFR1). (R) The mRNA expression of VEGFA in normal and ccRCC tissues based on the CPTAC database. (S) The protein expression of VEGFA in normal and ccRCC tissues based on the CPTAC database. (T) Available pathology images of VEGFA localization and expression in normal and ccRCC were obtained from the HPA database. Scale bar = 200 μm. $^{**}p < 0.01$, and $^{***}p < 0.001$.

senescence, epithelial/endothelial cell regulation, and VEGF signaling (Figure 6J,K). Proteomic data corroborated these findings, showing upregulation of FLT1, AKT1, and VEGFA proteins in ccRCC and association with various immune cells (Figure 6L,M). Correlation analyses further detailed the relationship between VEGFA/FLT1/AKT1 and other key genes in ccRCC and senescence, suggesting a complex regulatory interplay (Figures 6N,O and S10). Collectively, these multi-omics results support the model that a FLT1-centered regulatory network is critically involved in the cellular senescence program during ccRCC progression. Proteomics-based enrichment analysis further reinforced the association of this FLT1-associated profile with endothelial cell behaviors (e.g., migration, vascular transport) and epithelial cell behaviors (e.g., adhesion, differentiation) (Figure 6P,Q), underscoring its potential significance in the ccRCC microenvironment.

3.7 | The FLT1-Centered Regulatory Network Governs Endothelial-Epithelial Crosstalk

Based on previous findings, we further investigated the localization and functional relevance of FLT1 and its associated factors (VEGFA, AKT1) within key cell populations of ccRCC. Single-cell projection indicated that components of this FLT1-centered network (VEGFA, FLT1, AKT1) are overexpressed in ccRCC compared to normal tissues, with FLT1 and AKT1 primarily expressed in endothelial cells and VEGFA predominantly in epithelial cells (Figure 7A). Spatial transcriptomics, which preserves the spatial context of gene expression, allowed us to further dissect the distribution of the FLT1-centered regulatory network in situ. Our analysis delineated the spatial architecture of key cell populations in ccRCC. We visualized the spatial distribution of these populations alongside the expression patterns of the network components—FLT1, AKT1, and VEGFA (Figure 7B). The results revealed widespread high expression of this network within ccRCC neoplastic tissues. Specifically, FLT1 and AKT1 were predominantly localized to endothelial cell regions, whereas VEGFA was primarily enriched in epithelial cell areas. This spatial expression pattern strongly corroborates our findings from single-cell RNA sequencing analysis.

To validate and consolidate these multi-omics findings, we conducted immunofluorescence co-staining experiments (Figure 7C). By selecting the endothelial cell-specific marker CD34 for co-staining with FLT1 and AKT1, we visually confirmed the high expression of FLT1 and AKT1 in endothelial cell populations, a result consistent with expectations and reinforcing their potential role in tumor angiogenesis. Concurrently, for epithelial cells, we used KRT8 (as a marker for malignant epithelial cells [43]) for co-staining with VEGFA. The results not only verified the significant enrichment of VEGFA in ccRCC epithelial cells but also suggested that VEGFA may act as a key molecule regulating the behavior of these malignant epithelial cells. The notable upregulation of KRT8 further emphasized the importance of malignant epithelial cells in the pathological process of ccRCC and the regulatory role of VEGFA (Figure 7D). RT-qPCR results also confirmed that AKT1, CD34, VEGFA, and KRT8 were upregulated in ccRCC tissues compared to normal tissues (Figure 7E). To functionally test the predicted epithelial-endothelial crosstalk, we established a co-culture system. Conditioned medium from VEGFA-stimulated epithelial cells significantly upregulated the expression of FLT1, AKT1, as well as the downstream factors EGR1 and MMP9 in endothelial cells, compared to the control medium (Figure 7F). These orthogonal validation approaches, including spatial protein detection, transcriptional quantification in clinical samples, and functional co-culture assays, consistently support the existence and activity of the FLT1-centered network within the ccRCC tumor microenvironment.

3.8 | Exploring the Role of the FLT1-Centered Network in Endothelial and Epithelial Cell Subpopulations

To investigate the FLT1-centered regulatory network at higher resolution, we stratified key cellular populations (endothelial and epithelial cells) into subtypes. The endothelial cells were categorized into vein, capillary, and artery subtypes, while the epithelial cells were divided into PCT (proximal convoluted tubule), CFH (complement factor H), CD-ICA (collecting duct-Type A intercalated cells), and CD-ICB (collecting duct-Type B intercalated cells) (Figure 8A,B,E,F). Single-cell projection

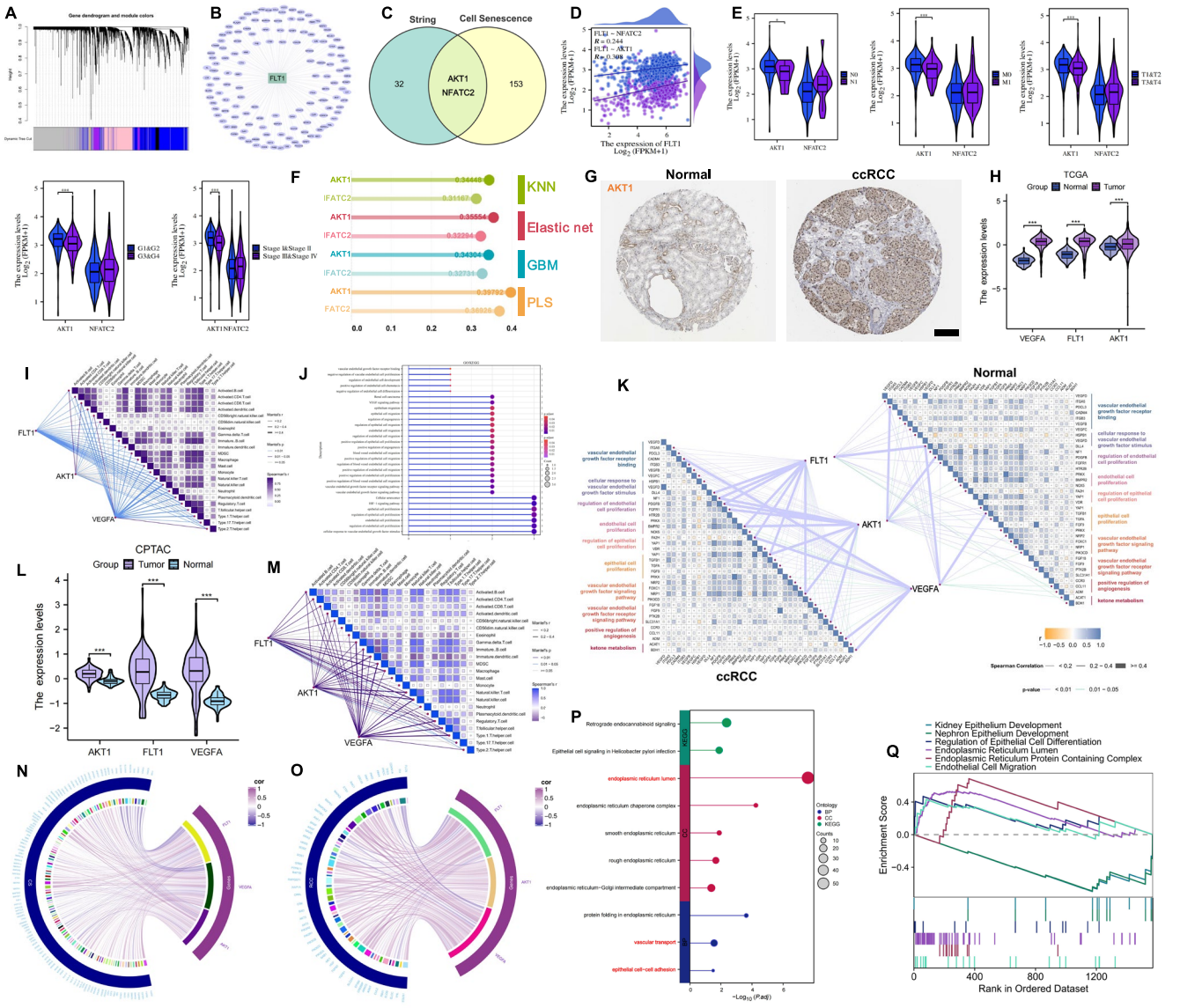

FIGURE 6 | Identification of the cellular senescence-related FLT1-centered regulatory network in ccRCC. (A) Cluster dendrogram of the co-expression network modules. (B) Key module genes-related FLT1. (C) Venn diagrams showed the most relative cellular senescence genes of FLT1. (D) Correlation analysis of FLT1, AKT1 and NFATC2. (E) Comparison of AKT1 and NFATC2 expression levels across different clinical characteristic groups in ccRCC. (F) KNN, Elastic net, GBM and PLS identified the key gene related FLT1. (G) Available pathology images of AKT1 localization and expression in normal and ccRCC were obtained from the HPA database. Scale bar = 200 μm. (H) Different expression level of the FLT1-centered regulatory network between normal and ccRCC groups. (I) Correlation analysis of the FLT1-centered regulatory and immune cells based on transcriptomics analysis. (J) GO and KEGG enrichment analysis of the FLT1-centered regulatory network based on transcriptomics analysis. (K) Correlations analysis of the FLT1-centered regulatory network and certain signaling pathways. (L) The protein expression of the FLT1-centered regulatory network between normal and ccRCC groups. (M) Correlation analysis of the FLT1-centered regulatory network and immune cells based on proteomics analysis. (N) Correlation analysis of the FLT1-centered regulatory network and cellular senescence-related genes. (O) Correlation analysis of the FLT1-centered regulatory network and RCC-related genes. (P) GO and KEGG enrichment analysis of the FLT1-centered regulatory network based on proteomics analysis. (Q) GSEA enrichment analysis of the FLT1-centered regulatory network based on proteomics analysis. *$p < 0.05$, **$p < 0.01$, and ***$p < 0.001$.

analysis revealed that FLT1 and AKT1 are widely distributed among endothelial cells, whereas VEGFA is predominantly expressed in the PCT and CFH subgroups of epithelial cells in ccRCC tissues compared to normal tissues (Figure 8C,D,G,H). These cell subpopulations with high expression of the VEGFA/FLT1/AKT1 axis may be potential malignant cell groups, and we will further explore them.

CellChat analysis indicates that, compared with normal tissues, the communication between the epithelial-endothelial cell subpopulations in ccRCC tissues is significantly enhanced (Figure 8I,J). To further elucidate the interactive mechanisms between endothelial cells mediated by FLT1 and AKT1, and epithelial cells mediated by VEGFA, we have categorized the endothelial cells into distinct subsets as follows:

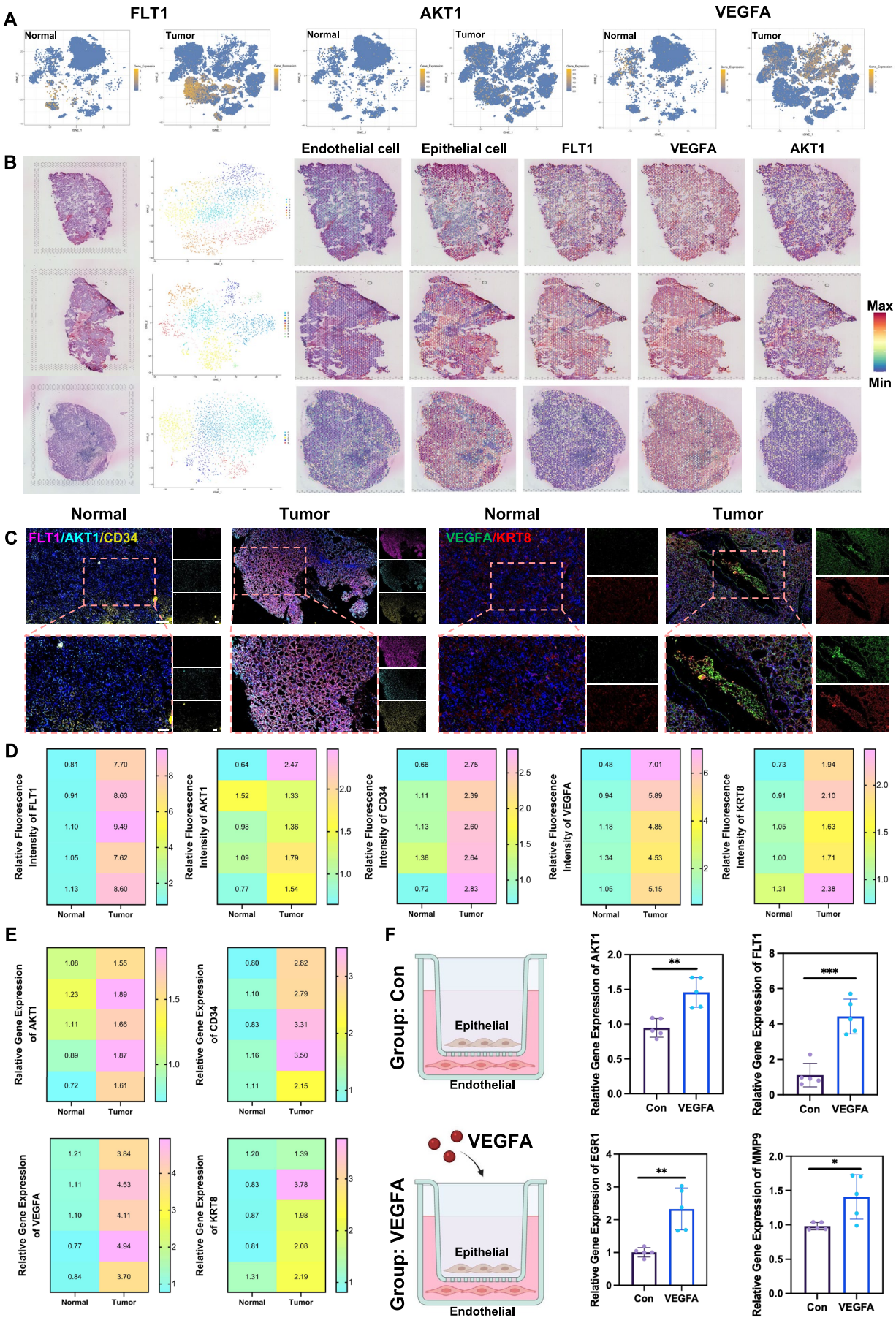

FIGURE 7 | Legend on next page.

FIGURE 7 | The FLT1-centered regulatory network mediates the behavior of endothelial and epithelial cells. (A) Expression of the FLT1-centered regulatory network in different cell clusters. (B) The spatial distribution of key cell clusters, FLT1, AKT1, and VEGFA. (C) Immunofluorescence images for the localization and the expression of FLT1/AKT1/CD34/VEGFA/KRT8 in HNSCC clinical samples. $n = 5$ per group. Scale bar = 200 μm (upper)/100 μm (lower). (D) Quantitative analysis of FLT1/AKT1/CD34/VEGFA/KRT8 intensity. (E) The relative expression levels of AKT1, CD34, VEGFA, and KRT8 in ccRCC clinical samples. $n = 5$ per group. (F) Endothelial cells were co-cultured with conditioned medium from epithelial cells treated with or without VEGFA. The relative expression levels of AKT1, FLT1, EGR1, and MMP9 in endothelial cells were measured by RT-qPCR. Groups: VEGFA (epithelial cells stimulated with VEGFA), Con (epithelial cells without VEGFA stimulation). *$p < 0.05$, **$p < 0.01$, and ***$p < 0.001$.

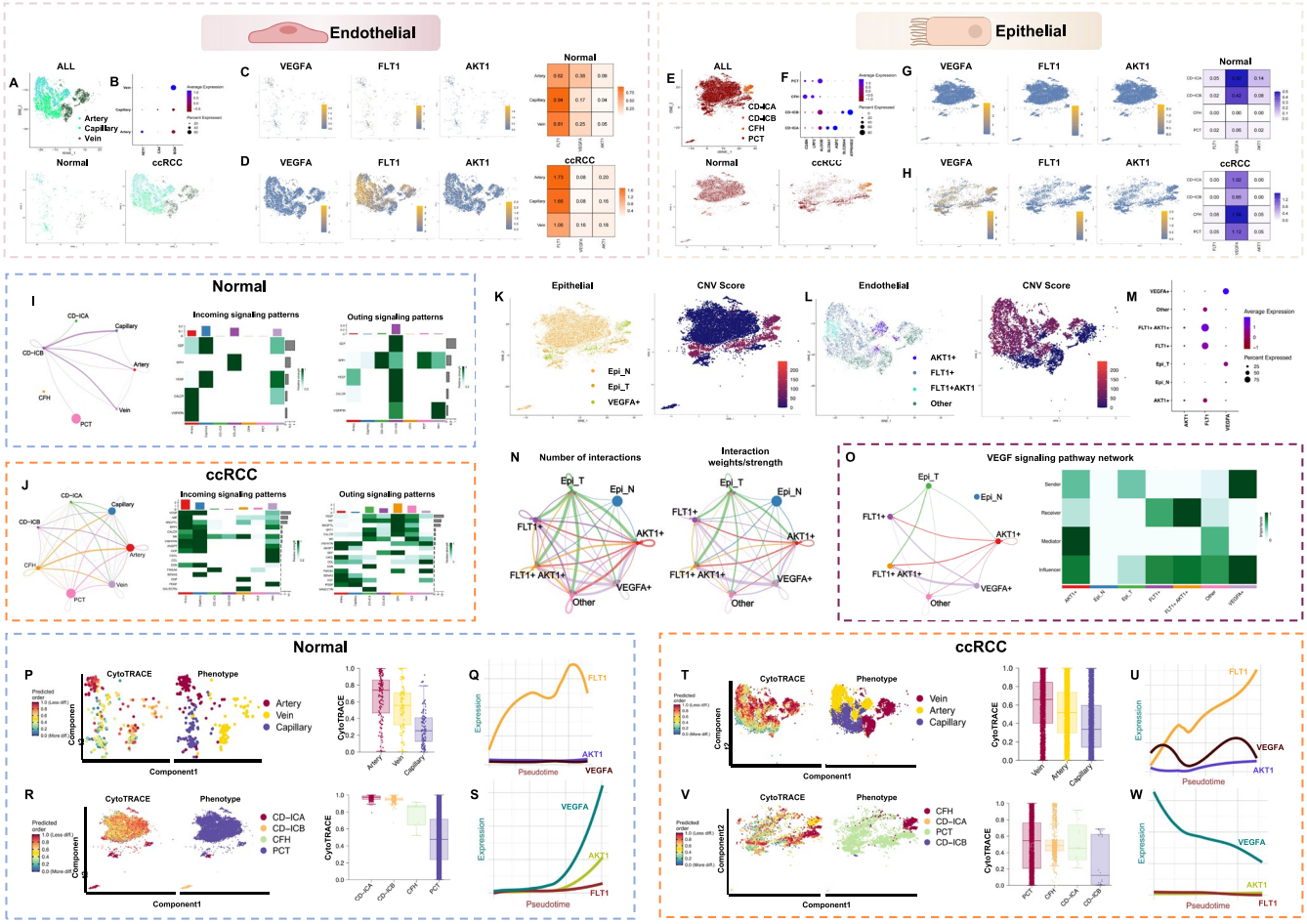

FIGURE 8 | The key role of the FLT1-centered regulatory network in endothelial and epithelial cell subsets. (A) tSNE of endothelial cells in ccRCC. (C) Marker genes in endothelial cell subsets. (C) Expression of the FLT1-centered regulatory network in endothelial cells in normal tissues. (D) Expression of the FLT1-centered regulatory network in endothelial cells in ccRCC tissues. (E) tSNE of epithelial cells in ccRCC. (F) Marker genes in epithelial cell subsets. (G) Expression of the FLT1-centered regulatory network in epithelial cells in normal tissues. (H) Expression of the FLT1-centered regulatory network in epithelial cells in ccRCC tissues. (I) CellChat analysis of cell subsets in normal tissues. (J) CellChat analysis of cell subsets in ccRCC tissues. (K) tSNE and CNV score of epithelial cells in ccRCC based on VEGFA expression. (L) tSNE and CNV score of endothelial cells in ccRCC based on FLT1 and AKT1 expression. (M) Expression of the FLT1-centered regulatory network in epithelial and endothelial cells. (N) CellChat analysis of endothelial and epithelial cell subsets. (O) The VEGF signaling pathway network of endothelial and epithelial cell subsets. (P) CytoTRACE score of endothelial cell subsets in normal tissues. (Q) Expression of the FLT1-centered regulatory network in endothelial cell subsets in normal tissues. (R) CytoTRACE score of epithelial cell subsets in normal tissues. (S) Expression of the FLT1-centered regulatory network in epithelial cell subsets in normal tissues. (T) CytoTRACE score of endothelial cell subsets in ccRCC tissues. (U) Expression of the FLT1-centered regulatory network in endothelial cell subsets in ccRCC tissues. (U) CytoTRACE score of epithelial cell subsets in ccRCC tissues. (W) Expression of the FLT1-centered regulatory network in epithelial cell subsets in ccRCC tissues.

FLT1-positive endothelial cells, AKT1-positive endothelial cells, FLT1- and AKT1-double-positive endothelial cells, and other. Correspondingly, epithelial cells have been classified into Epi_N, Epi_T, and VEGFA-positive epithelial cells. InferCNV is a tool that can identify chromosomal region amplifications or deletions by comparing differences in expression levels, thereby detecting malignant cells [44]. In our study, we scored the copy number variations (CNVs) for both endothelial and epithelial cells (Figures 8K–M and S12A). The results showed that in epithelial cells, those with high expression of VEGFA

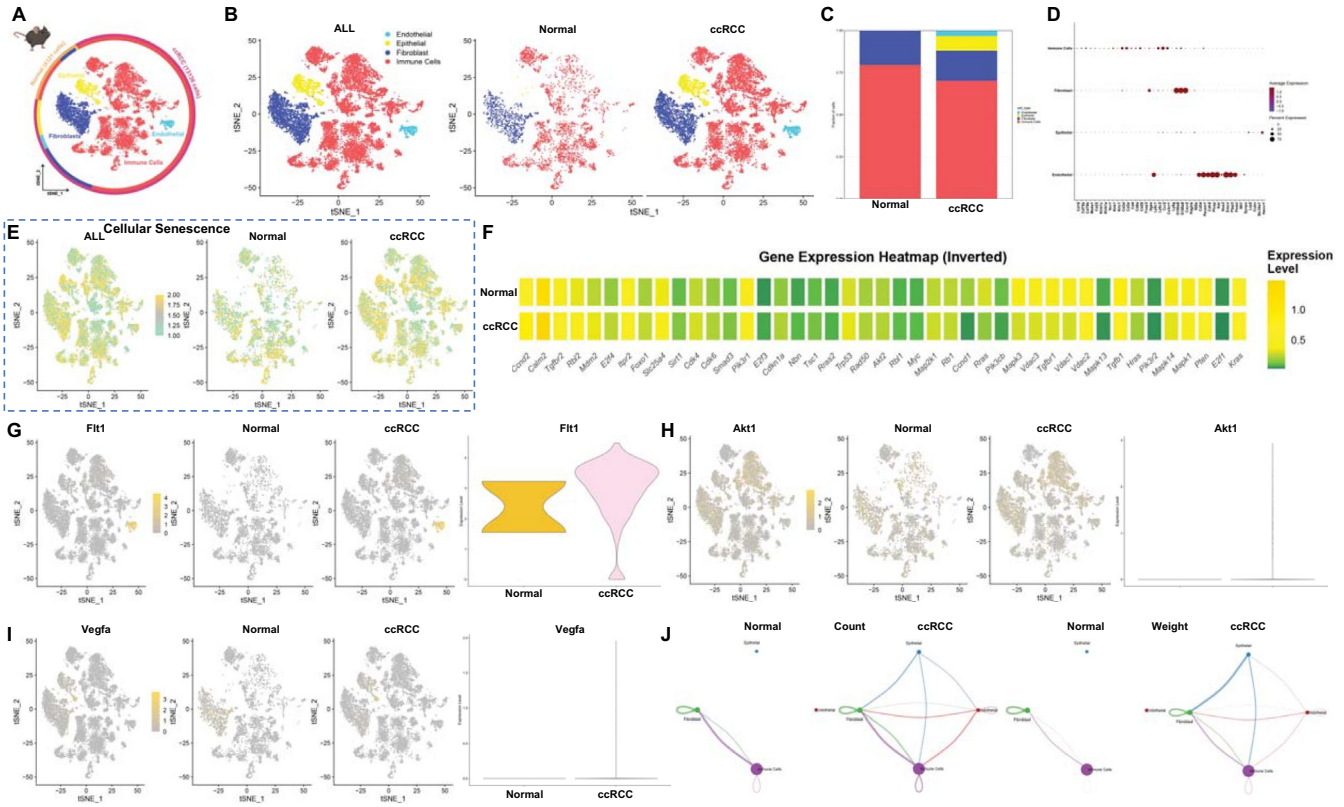

FIGURE 9 | Identification of the conserved FLT1-centered regulatory network in ccRCC across species through mouse scRNA-seq analysis. (A, B) tSNE representation of major cell types identified by scRNA-seq. (C) Bar graph of relative cell proportions. (D) Marker genes expressed in 4 major cell types. (E) Cellular senescence level of various cell types using the "AUcell" algorithm. (F) Heatmap of cellular senescence-related genes. (G) Expression of Flt1 is shown in tSNE. (H) Expression of Akt1 is shown in tSNE. (I) Expression of Vegfa is shown in tSNE. (J) CellChat analysis in normal and ccRCC groups.

had significantly higher CNV scores compared to other cells. In endothelial cells, we observed that cells with high expression of AKT1, high expression of FLT1, and co-expression of both AKT1 and FLT1 had significantly higher CNV scores compared to other cells. The CellChat analysis indicated that these malignant cells interact frequently, with the VEGF signaling pathway primarily mediating the interactions between epithelial and endothelial cells (Figures 8N,O and S12B,C). Therefore, we believe that endothelial cells with high activation of FLT1/AKT1 and epithelial cells with high activation of VEGFA are key malignant cell populations in ccRCC, and their frequent interactions are a critical reason for the progression of ccRCC. Through copy number variation (CNV) scoring, we have further identified the subpopulations of endothelial and epithelial cells that mediate malignant behaviors, which will aid in the design of more precise targeted treatment strategies: targeting the suppression of cells with high expression levels of VEGFA/FLT1/AKT1.

Pseudo-time analysis, based on the "CytoTRACE" algorithm, illustrates the differentiation process of cellular subgroups. In normal tissue, artery endothelial cells have higher CytoTRACE scores, indicating greater differentiation potential and gradually differentiating towards vein and capillary directions (Figure 8P). During this process, FLT1 fluctuates upwardly, while AKT1 and VEGFA are almost not expressed (Figure 8Q). In normal epithelial tissue, CD-ICA has higher CytoTRACE scores and better differentiation potential, gradually differentiating towards CD-ICB, CFH, and PCT (Figure 8R). During this differentiation, the expression of VEGFA, AKT1, and FLT1 rises progressively (Figure 8S). In the ccRCC tissue, a distinct abnormal cell differentiation trend was observed, along with the gene expression pattern of the VEGFA/FLT1/AKT1 axis. Endothelial cells differentiate from vein towards artery and capillary directions, and epithelial cells differentiate from PCT towards CFH, CD-ICA, and CD-ICB directions (Figure 8T,V). Venous endothelial cells are the starting point for tumor angiogenesis [45], and our results indicated that in ccRCC, endothelial cell subpopulations were differentiating from venous endothelial cells to other subpopulations, suggesting that there was a significant amount of new tumor blood vessel formation in ccRCC. Furthermore, as the cells of origin for ccRCC, PCT cells are observed to be differentiating into other cell populations within ccRCC [46]. Furthermore, during the differentiation process, a continuous increase in FLT1 expression, fluctuating VEGFA expression, and a slow increase in AKT1 expression were observed in the endothelial cell subpopulations, which were different from those in normal tissues (Figure 8U). Among the epithelial cell subgroups, as differentiation proceeds, it was observed that the expression of VEFGA gradually decreases, while AKT1 and FLT1 show almost no significant expression, which were also different from that in normal tissues (Figure 8W). Therefore, by understanding the differentiation process of ccRCC cell subpopulations and inhibiting the trend of cell subpopulations differentiating into malignant cells, it may help to reverse the poor outcomes associated with the prognosis of ccRCC.

3.9 | Conservation of the FLT1-Centered Regulatory Network in ccRCC Across Species

To investigate whether the FLT1-associated regulatory network identified in human ccRCC is evolutionarily conserved, we analyzed single-cell RNA-seq data from a mouse ccRCC model. Compared with normal tissues, a group of epithelial cells and endothelial cells were significantly present in the tumor tissues (Figures 9A–D and S13). The cellular senescence-related gene set showed a globally higher projection in the tumor samples, although the specific genes exhibited different expression patterns between the two groups (Figure 9E,F). Focusing on the key components (Vegfa, Flt1, and Akt1), we observed conserved expression patterns: Flt1 and Akt1 were predominantly localized to endothelial cells, while Vegfa was mainly expressed in epithelial cells within mouse ccRCC (Figure 9G–I). In ccRCC, close interactions were also directly observed between the epithelial cells and the endothelial cells, as well as between these cells and other cell types (Figure 9J).

Similarly, we further conducted an analysis on the subgroups of endothelial cells and epithelial cells. Endothelial cells were classified into three subtypes: artery, capillary, and vein, with Flt1 and Akt1 widely distributed in each of these subtypes (Figure 10A–D). There are frequent interactions among different endothelial cell subsets in ccRCC (Figure 10E). The pseudotime and CytoTRACE analyses of the differentiation potential of endothelial cells revealed that capillary cells exhibited the highest differentiation potential among the three types of cells, which seems to be inconsistent with the results obtained from human samples (Figure 10F–H). However, we also observed that the expression of Flt1 in mouse endothelial cells showed a significant change as well, and its expression peak occurred in the capillary subpopulation, which is highly consistent with the findings in human samples (Figure 10I). Epithelial cells are classified into three subtypes: EMT_epi, Proximal_tubule, and T_epi (Figure 10J–L). Among them, Vegfa is predominantly highly expressed in T_epi (Figure 10M). Proximal_tubule and T_epi maintain a close interaction relationship with EMT_epi in ccRCC (Figure 10N). The pseudo-time and CytoTRACE analyses revealed the differentiation trend and direction from T_epi to Proximal_tubule and finally to EMT_epi in mouse epithelial cells (Figure 10O–Q). Vegfa, as a key gene in the previously identified epithelial cell subgroups, was found to be increasingly expressed during the differentiation process (Figure 10R).

Collectively, the mouse ccRCC data support the conservation of a FLT1-centered regulatory network involving Vegfa and Akt1, with similar cellular expression patterns and evidence of active epithelial-endothelial crosstalk, underscoring its potential fundamental role in ccRCC pathobiology across species.

3.10 | Drug Sensitivity and Immunotherapeutic Analysis of the FLT1-Centered Regulatory Network

Having elucidated the role of the FLT1-centered regulatory network in senescence-related pathways, we further investigated its clinical implications regarding drug sensitivity and immunotherapy response, aiming to inform personalized treatment strategies for ccRCC patients exhibiting dysregulation of this network. We first compared the immune phenotype score (IPS) between patient subgroups defined by high versus low expression of the FLT1-associated gene signature (including FLT1, VEGFA, and AKT1). Results indicated that patients with low expression of this signature consistently exhibited higher IPS across all evaluated subgroups (CTLA4-PD1-, CTLA4-PD1+, CTLA4+ PD1-, and CTLA4+ PD1+), suggesting a potentially better response to immune checkpoint blockade therapy. Conversely, patients with high expression of this network may require alternative or combinatorial therapeutic approaches (Figure 11A). Subsequently, we screened the ChEMBL database for drugs known to inhibit targets within this FLT1-centered network and clinically validated in cancer therapy (Figure 11B). Ten drugs targeting FLT1 demonstrated excellent binding stability (Figure 11C). The binding structure of the FLT1-associated gene signature with key drugs was visually presented (Figure 11D–O). In order to verify the molecular docking simulation results of FLT1 and the targeted drugs, molecular dynamics simulations were conducted for the five most stable complexes. Gibbs energy landscapes and RMSD curves of the complexes formed by the five drugs and FLT1 are shown (Figure 11P–T). In the Gibbs energy landscape, the dark blue regions represent areas of lower energy, which are the stable states of FLT1-drug binding. During the simulation, the FLT1-Lenvatinib and FLT1-Pazopanib complexes mainly adopt two primary low-energy conformations, while the FLT1-Fruquintinib, FLT1-Regorafenib, and FLT1-Sorafenib complexes mainly adopt one primary low-energy conformation. This indicates that they have relatively stable binding modes in the sampled conformational landscape. RMSD analysis revealed all five complexes achieved stable binding after a brief fluctuation, which was confirmed in the MMGBSA (Figure 11U,V). Supplementary analyses of solvent-accessible surface area (SASA), gyration radius (Rg), RMSF, and hydrogen bonding number provided further structural insights. Conversely, they all exhibit reliable binding with FLT1, especially Sorafenib, Regorafenib, and Lenvatinib (Figure 11W–Z).

4 | Discussion

ccRCC is the most common type of kidney cancer, and its rising incidence poses an increasingly serious challenge to global human health [47]. Previous cancer research has mainly focused on the tumor cells themselves, without fully considering the complex interactions between tumor cells and their surrounding microenvironment, which has limited our in-depth understanding of tumor heterogeneity. Senescent cells, once considered "zombie cells," neither proliferate nor undergo death but persist in tissues, absorbing nutrients from the microenvironment and excreting waste through metabolism [48]. As a result, senescent cells have not received enough attention in previous research. However, recent studies have found that they play an active role in various physiological processes, including natural aging, embryonic development, wound healing, tissue regeneration, and the occurrence of tumors [49]. Especially in the field of cancer, the introduction of cellular senescence therapy has opened up new avenues for cancer treatment. Senescence dissolution therapy can selectively eliminate senescent cells, while senescence morphology therapy inhibits the production and secretion of SASP, disrupting the pro-inflammatory characteristics of senescent cells and promoting the normalization of the SASP process

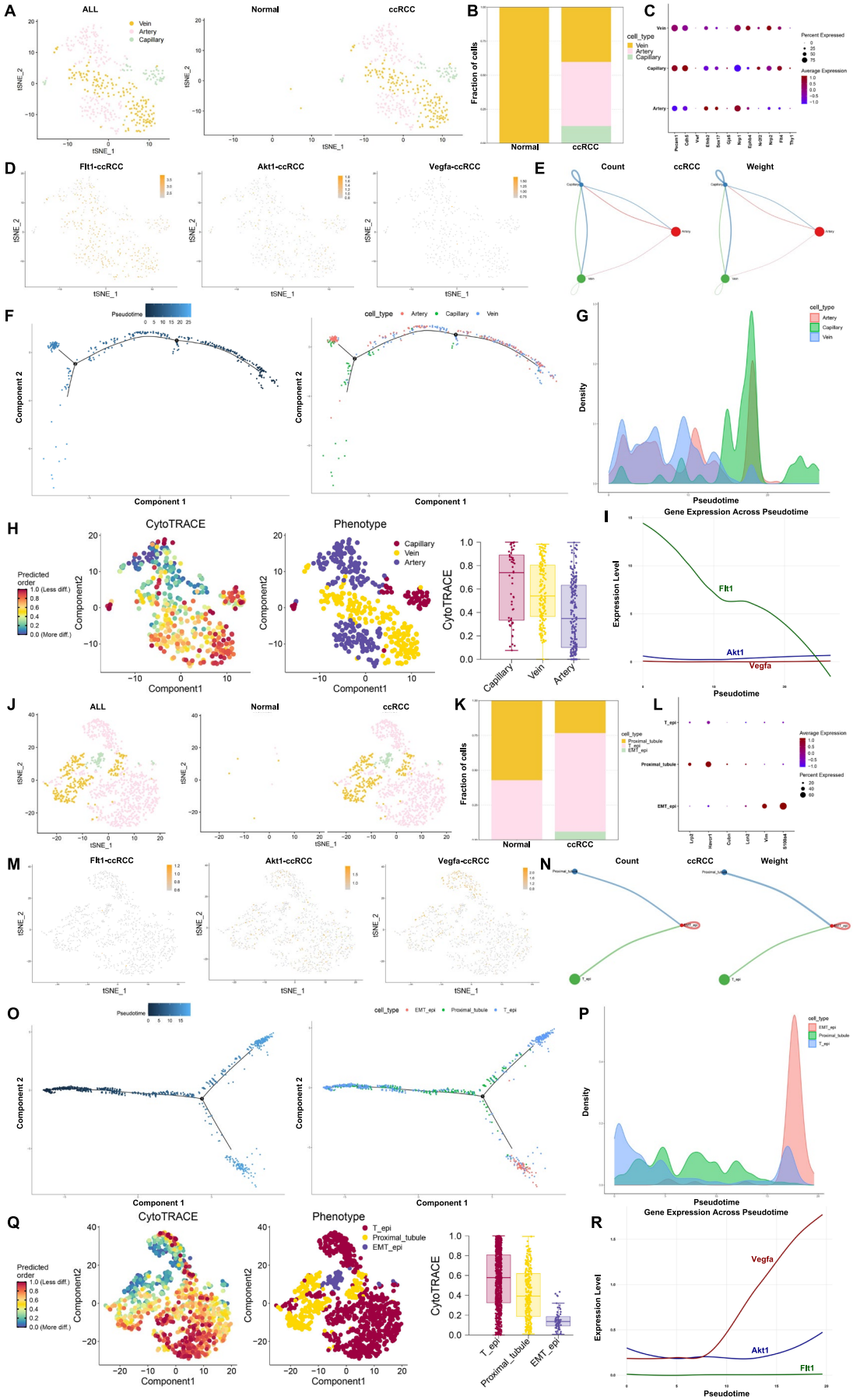

FIGURE 10 | Legend on next page.

FIGURE 10 | The key role of the Flt1-centered regulatory network in endothelial and epithelial cell subsets in mouse. (A) tSNE of endothelial cells. (B) Bar graph of relative endothelial cell proportions. (C) Marker genes in endothelial cell subsets. (D) Expression of the Flt1-centered regulatory network in endothelial cells in ccRCC tissues. (E) CellChat analysis of endothelial cells in ccRCC. (F, G) Pseudo-time analysis of endothelial cells in ccRCC. (H) CytoTRACE score of endothelial cell subsets in ccRCC tissues. (Q) Expression of the Flt1-centered regulatory network in endothelial cell subsets in ccRCC tissues. (J) tSNE of epithelial cells. (K) Bar graph of relative epithelial cell proportions. (L) Marker genes in epithelial cell subsets. (M) Expression of the Flt1-centered regulatory network in epithelial cells in ccRCC tissues. (N) CellChat analysis of epithelial cells in ccRCC. (O, P) Pseudo-time analysis of epithelial cells in ccRCC. (Q) CytoTRACE score of epithelial cell subsets in ccRCC tissues. (R) Expression of the Flt1-centered regulatory network in epithelial cell subsets in ccRCC tissues.

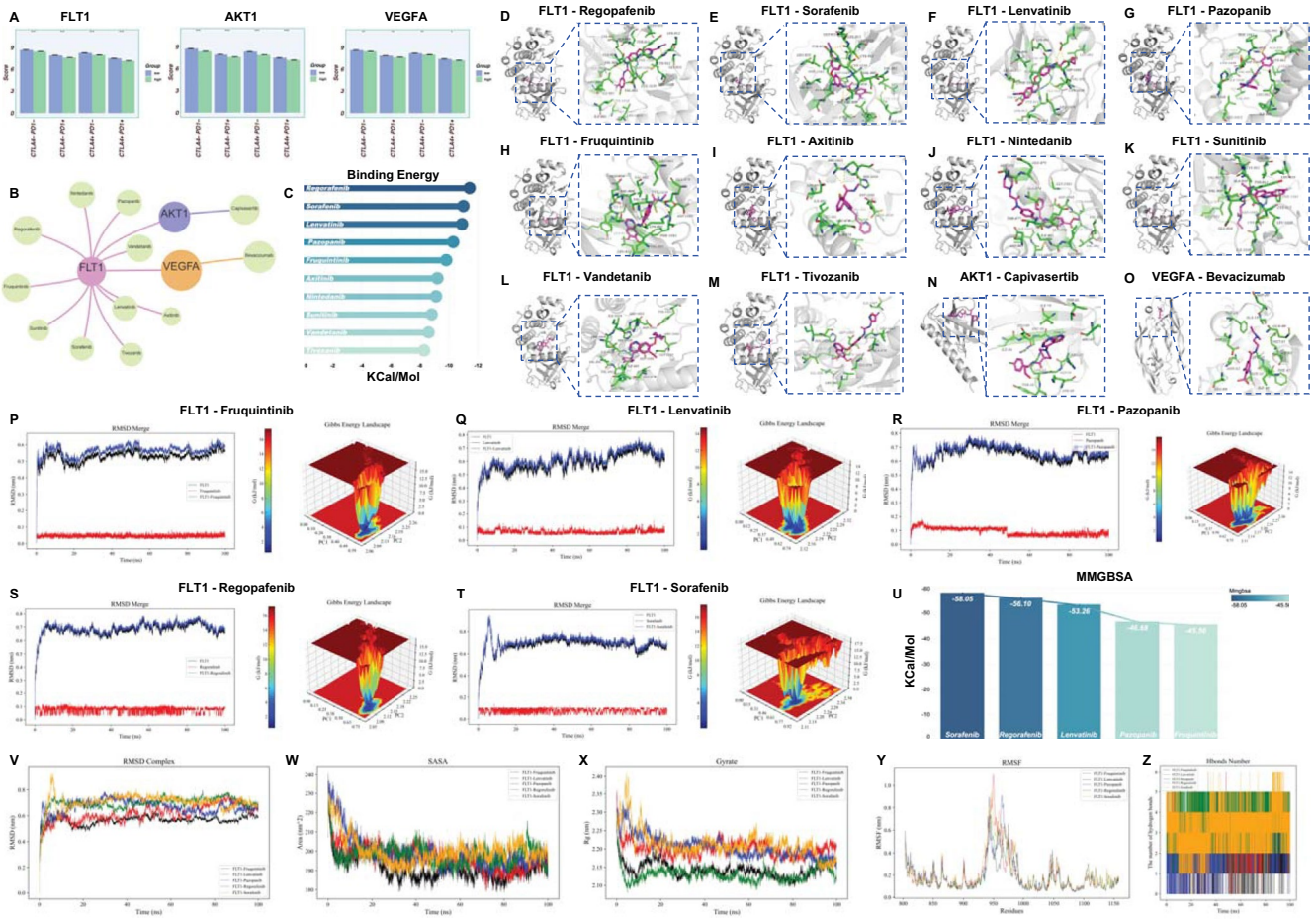

FIGURE 11 | Integrations of drug sensitivity data with in molecular docking analyses to identify candidate drugs targeting the FLT1-centered regulatory network. (A) IPS score of patients with ccRCC with low- and high-VEGFA/FLT1/AKT1 axis expression in the CTLA4- PD1-, CTLA4- PD1+, CTLA+ PD1-, and CTLA+ PD1+ subgroups. (B) Candidate FDA-approval drugs of the FLT1-centered regulatory network. (C) Binding energy of FLT1-related drugs. (D-O) Molecular docking simulating the combine effects of drugs between the FLT1-centered regulatory network and key drugs. (P) Gibbs Energy landscape diagrams show the stability of FLT1–Fruquintinib complexes. (Q) Gibbs Energy landscape diagrams show the stability of FLT1–Lenvatinib complexes. (R) Gibbs Energy landscape diagrams show the stability of FLT1–Pazopanib complexes. (S) Gibbs Energy landscape diagrams show the stability of FLT1–Regorafenib complexes. (T) Gibbs Energy landscape diagrams show the stability of FLT1–Sorafenib complexes. (U) MMGBSA of FLT1-related drugs. (V–Z) Line plots present dynamic simulation metrics (e.g., RMSD, Gyrate, hydrogen bond numbers, RMSF, SASA) over time. *$p < 0.05$, **$p < 0.01$, and ***$p < 0.001$.

in the senescent microenvironment [50]. With the rapid development of omics technologies in recent years, we can now more comprehensively examine the complexity of the tumor microenvironment and deeply analyze the interactions and dynamic changes between tumor cells [27, 51, 52]. In this study, we have preliminarily confirmed the negative role of cellular senescence in ccRCC using transcriptomics and single-cell analysis techniques. The study found that the expression of multiple genes related to cellular senescence was abnormal in ccRCC, and the increase in the level of cellular senescence is closely related to poor clinical prognosis in ccRCC. In addition, we further analyzed the interrelationships between cellular senescence and various components of the tumor microenvironment, and we found that the level of cellular senescence is not only related to the expression level of immune cells but also closely connected to the activation status of multiple signaling pathways. These

findings suggest that cellular senescence may affect the progression of ccRCC through various mechanisms, such as immune evasion, promoting angiogenesis, and enhancing the invasiveness of tumor cells, and the specific mechanisms still need further exploration.

Given the importance of cellular senescence in ccRCC, we have constructed a prognostic signature related to senescence-associated genes to assess the prognosis of ccRCC patients. We found that multiple immune response pathways are activated in the low-risk group, while multiple cancer-related pathways are activated in the high-risk group. Additionally, we discovered that patients in the low-risk group have a lower TMB and a higher rate of immune cell infiltration. These findings suggest that patients in the low-risk group may respond better to immunotherapy, while those in the high-risk group require further exploration of other effective therapeutic targets [53]. We have used a variety of machine learning algorithms to identify the most critical gene, FLT1. FLT1, also known as VEGFR1, is a vascular endothelial growth factor receptor that promotes angiogenesis upon binding with vascular endothelial growth factor, which is crucial for tumor angiogenesis. Beyond its role as a receptor for vascular endothelial growth factor, FLT1 also modulates the vascular endothelial growth factor signaling pathway through different mechanisms [54]. For instance, FLT1 can form an ineffective VEGF-FLT1 complex to compete with VEGFR2 for VEGF binding, thereby regulating the intensity and duration of VEGF signal transduction [55]. The expression of FLT1 is closely related to the aggressiveness and prognosis of tumors, with high expression levels usually associated with a poorer prognosis [56]. Our study also confirmed FLT1 is highly expressed in tumor tissues and is a good potential regulatory target.

To further elucidate the specific regulatory mechanisms of FLT1 in the development of ccRCC, we applied a multitude of machine learning methods and multi-omics analyses. Through this approach, we identified FLT1 as a central regulator within a network that also involves VEGFA and AKT1, which appears to govern endothelial-epithelial cell behavior in the context of cellular senescence in ccRCC. Immunofluorescence co-staining and RT-qPCR have corroborated the multi-omics findings, indicating that this FLT1-centered network is highly activated in ccRCC tissues and mediates malignant cellular behavior and interactions between endothelial and epithelial cells. Previous studies have confirmed that AKT1 functions as a downstream gene of FLT1, and the VEGFA/FLT1/AKT1 regulatory axis can affect cell survival [57–59]. Moreover, VEGFA, FLT1, and AKT1 have all been proven to be genes related to cellular senescence [60–62]. In particular, AKT1 is involved in multiple processes of cellular senescence, such as regulating cell cycle-related proteins, participating in the cell's response to oxidative stress, affecting telomere length, and regulating intracellular metabolism and energy balance [57]. This leads us to propose a model wherein epithelial-derived VEGFA activates the FLT1-centered regulatory network on endothelial cells to foster a pro-tumorigenic microenvironment. Our in vitro functional studies provide direct experimental support for this model. siRNA-mediated knockdown of FLT1 in 786-O cells not only attenuated their malignant phenotypes but also significantly downregulated the expression of key senescence markers (e.g., CDKN1A/p21, CDKN2A/p16) and SASP factors [63, 64], functionally linking FLT1 activity to the senescence program in ccRCC. To validate the predicted epithelial-endothelial crosstalk, we established a co-culture system. We found that conditioned medium from VEGFA-stimulated epithelial cells specifically upregulated the expression of FLT1, AKT1, and their downstream effectors EGR1 and MMP9 in endothelial cells [65, 66]. This result provides direct evidence that an epithelial-derived signal (VEGFA) can activate the FLT1/AKT1 expression levels in neighboring endothelial cells. Collectively, these data position the FLT1-centered network as a key functional mediator in the senescence-associated microenvironment of ccRCC, moving beyond correlative observation to mechanistic insight.

We further explored the key roles of the FLT1-associated gene signature in endothelial and epithelial cells. Tumor endothelial cells are considered a key cell population in promoting angiogenesis, and anti-angiogenic therapy is a main strategy for the treatment of advanced ccRCC. Endothelial cells are heterogeneous, and different subsets of ECs may respond differently to anti-angiogenic drugs [67]. This could mean that some drugs are only effective against specific cell subsets. Therefore, a thorough understanding of the characteristics of different endothelial cell subsets is necessary to develop more precise drugs that target the cells that play a crucial role in tumor angiogenesis. Previous studies have suggested that endothelial cells compete for the position of migratory tip cells (guiding and navigating the vessel sprout) based on the relative levels of VEGFR1 (FLT1) and VEGFR2 [68]. Previous studies have also confirmed that tumor angiogenesis begins with venous endothelial cells [45]. Our pseudo-time analysis results revealed that endothelial cell subpopulations gradually differentiate from venous endothelial cells towards other subpopulations, with the expression of AKT1 and FLT1 gradually increasing during the differentiation process. Combined with the CNV scoring results, it was shown that as the expression of AKT1 and FLT1 increases, endothelial cell subpopulations gradually exhibit malignant behaviors. We believe that in ccRCC, venous endothelial cells are actively differentiating into other cells, leading to a large amount of tumor angiogenesis, and the cell behavior is gradually transforming towards malignancy. By inhibiting endothelial cell subpopulations with high expression of AKT1 and FLT1, it is possible to precisely target malignant cell subpopulations, and by inhibiting the expression of AKT1 and FLT1, it may be possible to block the malignant differentiation process of endothelial cell subpopulations, preventing the progression of ccRCC.

Epithelial cells also play a key role in the development of ccRCC [69]. The proximal tubular epithelial cells are considered to be the cells of origin for ccRCC, but the mechanism of their transition from normal to malignant is not yet clear [46, 70]. Gaining insights into the tumor's genesis and its developmental trajectory is crucial for crafting targeted therapeutic approaches [71]. Pinpointing the cell of origin and the sequence of events leading to malignancy not only enhances our comprehension of cancer progression but also opens avenues for early intervention. Our research indicated that in normal tissue, the differentiation potential of proximal renal tubular epithelial cells was relatively low, but it significantly increased in ccRCC. These proximal renal tubular epithelial cells were actively transforming into other epithelial cell subpopulations. Additionally, we

have observed that the proximal renal tubular epithelial cells in ccRCC highly express VEGFA, which is associated with the highest degree of malignancy. The transition of proximal tubular epithelial cells from a normal state to a malignant state makes ccRCC more aggressive. Therefore, we believe that these proximal tubular epithelial cells with high VEGFA expression are the frontier cells in the malignant progression of ccRCC. By monitoring the expression of VEGFA, we can accurately identify the malignant origin of ccRCC. Inhibiting VEGFA may prevent the malignant progression of ccRCC and improve the prognosis of patients with ccRCC. Interestingly, we identified the conserved expression of the FLT1-centered regulatory network in mouse single-cell data, where this axis similarly plays a pivotal role in regulating malignant behaviors between endothelial and epithelial cells in mice. However, we observed that the expression dynamics of this signaling axis during the differentiation processes of endothelial and epithelial cell subsets exhibited an opposite trend compared to that in human tissue samples. These findings suggest that further in-depth exploration of the functional role of the FLT1-centered regulatory network should focus on human tissue samples to better understand its context-specific mechanisms.

The therapy suitable for each ccRCC patient may depend on the individual clinical and molecular characteristics of the tumor. Patients with ccRCC that have low expression of the FLT1-centered regulatory network may achieve a better therapeutic response from immunotherapy, while those with high expression of the FLT1-centered regulatory network will require finding other more effective treatment strategies [72]. A single targeted drug may be very effective initially, but it can quickly lead to drug resistance in patients, resulting in reduced efficacy. Combination therapy can help avoid drug resistance [73]. Therefore, we have designed a combined targeting treatment strategy for the FLT1-centered regulatory network, which can inhibit the malignant progression of ccRCC through various pathways by inhibiting the expression of VEGFA, FLT1, and AKT1, respectively. We identified FDA-approved drugs targeting the FLT1-centered regulatory network from the ChEMBL database and validated their binding stability through molecular docking and molecular dynamics simulations. The selected drugs included FLT1 inhibitors (sorafenib, regorafenib, and lenvatinib, an AKT1 inhibitor (capivasertib), and a VEGFA inhibitor (bevacizumab)). These are all clinically approved anti-cancer drugs that target distinct nodes within the FLT1-centered regulatory network. They have demonstrated clear anti-angiogenic or anti-tumor activity in a variety of solid tumors [74–78]. Therefore, as part of a "drug repurposing" strategy [79], the combined targeting of this signaling axis holds promise for providing more effective synergistic therapeutic approaches for ccRCC patients with abnormal overexpression of the FLT1-centered regulatory network.

Author Contributions

M.S. and Y.Z. contributed to the conception and design. H.M. and Y.L. collected and analyzed the data. Z.H., S.L., Z.L., L.P., Q.Z., and J.Z. drew the figures and tables. M.S., Y.L., and M.Y. wrote the draft. M.S. and Y.Z. contributed to manuscript writing and revision. All authors read and approved the final manuscript.

Funding

This work was financially supported by the following programs: Zhejiang Province Traditional Chinese Medicine Science and Technology Plan Project (2026ZL0078), National Natural Science Foundation of China (82501180), Zhejiang Provincial Natural Science Foundation of China (LQN25H140004, LY21H050006), China Postdoctoral Science Foundation (2023M743009, 2024T170782).

Ethics Statement

The study methods were in accordance with the ethical principles of "Ethical Review for Biomedical Research Involving Human Subjects" (2016), the National Health Commission of PRC, "Declaration of Helsinki" of WMA, and "International Ethical Guidelines for Human Biomedical Research" of CIOMS. The study involving human participants was reviewed and approved by the Ethics Committee in Clinical Research (ECCR) of the First Affiliated Hospital of Wenzhou Medical University. This study collected samples from 5–10 ccRCC patients during 2022–2024. Participants provided written informed consent to participate in this study. The ethics number was KY2021-160.

Conflicts of Interest

The authors declare no conflicts of interest.

Data Availability Statement

All data generated or analyzed during this study are included in this article and Supporting Information. The raw data and code are available from the corresponding author upon request.

References

1. J. Hu, S.-G. Wang, Y. Hou, et al., "Multi-Omic Profiling of Clear Cell Renal Cell Carcinoma Identifies Metabolic Reprogramming Associated With Disease Progression," *Nature Genetics* 56 (2024): 442–457, https://doi.org/10.1038/s41588-024-01662-5.

2. E. Jonasch, C. L. Walker, and W. K. Rathmell, "Clear Cell Renal Cell Carcinoma Ontogeny and Mechanisms of Lethality," *Nature Reviews Nephrology* 17 (2021): 245–261, https://doi.org/10.1038/s41581-020-00359-2.

3. J. R. Saout, G. Lecuyer, S. Léonard, et al., "Single-Cell Deconvolution of a Specific Malignant Cell Population as a Poor Prognostic Biomarker in Low-Risk Clear Cell Renal Cell Carcinoma Patients," *European Urology* 83 (2023): 441–451, https://doi.org/10.1016/j.eururo.2023.02.008.

4. D. Lu, Y. Li, X. Niu, et al., "STAT2/SLC27A3/PINK1-Mediated Mitophagy Remodeling Lipid Metabolism Contributes to Pazopanib Resistance in Clear Cell Renal Cell Carcinoma," *Research* 7 (2024): 0539, https://doi.org/10.34133/research.0539.

5. U. Capitanio and F. Montorsi, "Renal Cancer," *Lancet (London, England)* 387 (2016): 894–906, https://doi.org/10.1016/S0140-6736(15)00046-X.

6. J. J. Hsieh, M. P. Purdue, S. Signoretti, et al., "Renal Cell Carcinoma," *Nature Reviews. Disease Primers* 3 (2017): 17009, https://doi.org/10.1038/nrdp.2017.9.

7. W. K. Rathmell, R. B. Rumble, P. J. Van Veldhuizen, et al., "Management of Metastatic Clear Cell Renal Cell Carcinoma: ASCO Guideline," *Journal of Clinical Oncology: Official Journal of the American Society of Clinical Oncology* 40 (2022): 2957–2995, https://doi.org/10.1200/JCO.22.00868.

8. R. J. Motzer, E. Jonasch, N. Agarwal, et al., "Kidney Cancer, Version 3.2022," *Journal of the National Comprehensive Cancer Network* 20 (2022): 71–90, https://doi.org/10.6004/jnccn.2022.0001.

9. C. M. Díaz-Montero, B. I. Rini, and J. H. Finke, "The Immunology of Renal Cell Carcinoma," *Nature Reviews. Nephrology* 16 (2020): 721–735, https://doi.org/10.1038/s41581-020-0316-3.

10. A. Obradovic, N. Chowdhury, S. M. Haake, et al., "Single-Cell Protein Activity Analysis Identifies Recurrence-Associated Renal Tumor Macrophages," *Cell* 184 (2021): 2988–3005.e16, https://doi.org/10.1016/j.cell.2021.04.038.

11. Q. Liu and H. Ma, "Cancer Biotherapy: Review and Prospect," *Clinical and Experimental Medicine* 24 (2024): 114, https://doi.org/10.1007/s10238-024-01376-2.

12. Y. Zhou, L. Tao, J. Qiu, et al., "Tumor Biomarkers for Diagnosis, Prognosis and Targeted Therapy," *Signal Transduction and Targeted Therapy* 9 (2024): 1–86, https://doi.org/10.1038/s41392-024-01823-2.

13. M. Sun, N. Zhan, Z. Yang, et al., "Cuproptosis-Related lncRNA JPX Regulates Malignant Cell Behavior and Epithelial-Immune Interaction in Head and Neck Squamous Cell Carcinoma via miR-193b-3p/PLAU Axis," *International Journal of Oral Science* 16 (2024): 1–16, https://doi.org/10.1038/s41368-024-00314-y.

14. M. Binnewies, E. W. Roberts, K. Kersten, et al., "Understanding the Tumor Immune Microenvironment (TIME) for Effective Therapy," *Nature Medicine* 24 (2018): 541–550, https://doi.org/10.1038/s41591-018-0014-x.

15. R. Baghban, L. Roshangar, R. Jahanban-Esfahlan, et al., "Tumor Microenvironment Complexity and Therapeutic Implications at a Glance," *Cell Communication and Signaling* 18 (2020): 59, https://doi.org/10.1186/s12964-020-0530-4.

16. C. López-Otín, F. Pietrocola, D. Roiz-Valle, L. Galluzzi, and G. Kroemer, "Meta-Hallmarks of Aging and Cancer," *Cell Metabolism* 35 (2023): 12–35, https://doi.org/10.1016/j.cmet.2022.11.001.

17. H.-L. Ou, R. Hoffmann, C. González-López, G. J. Doherty, J. E. Korkola, and D. Muñoz-Espín, "Cellular Senescence in Cancer: From Mechanisms to Detection," *Molecular Oncology* 15 (2021): 2634–2671, https://doi.org/10.1002/1878-0261.12807.

18. T.-W. Kang, T. Yevsa, N. Woller, et al., "Senescence Surveillance of Pre-Malignant Hepatocytes Limits Liver Cancer Development," *Nature* 479 (2011): 547–551, https://doi.org/10.1038/nature10599.

19. T. Liu, X. Song, X. Dai, et al., "Effects of Animal-Derived Peptides on Aging-Related Diseases: A Narrative Review," *Aging Advances* 2 (2025): 160–165, https://doi.org/10.4103/AGINGADV.AGINGADV-D-25-00012.

20. I. Marin, O. Boix, A. Garcia-Garijo, et al., "Cellular Senescence Is Immunogenic and Promotes Antitumor Immunity," *Cancer Discovery* 13 (2023): 410–431, https://doi.org/10.1158/2159-8290.CD-22-0523.

21. V. Sorrenti, A. Buriani, S. Fortinguerra, et al., "Cell Survival, Death, and Proliferation in Senescent and Cancer Cells: The Role of (Poly) phenols," *Advances in Nutrition (Bethesda, Md.)* 14 (2023): 1111–1130, https://doi.org/10.1016/j.advnut.2023.05.014.

22. B. I. Pereira, O. P. Devine, M. Vukmanovic-Stejic, et al., "Senescent Cells Evade Immune Clearance via HLA-E-Mediated NK and CD8+ T Cell Inhibition," *Nature Communications* 10 (2019): 2387, https://doi.org/10.1038/s41467-019-10335-5.

23. L. Wang, L. Lankhorst, and R. Bernards, "Exploiting Senescence for the Treatment of Cancer," *Nature Reviews. Cancer* 22 (2022): 340–355, https://doi.org/10.1038/s41568-022-00450-9.

24. N. K. Sharma, "Common Molecular Basis of Aging and Cancer Dynamics: Complex Interactions Among Age, Diseases, External Stressors, and Environmental Factors," *Aging Advances* 1 (2024): 23–26, https://doi.org/10.4103/AGINGADV.AGINGADV-D-24-00003.

25. L. Wang, H. Jin, F. Jochems, et al., "cFLIP Suppression and DR5 Activation Sensitize Senescent Cancer Cells to Senolysis," *Nature Cancer* 3 (2022): 1284–1299, https://doi.org/10.1038/s43018-022-00462-2.

26. N. M. Anderson and M. C. Simon, "The Tumor Microenvironment," *Current Biology* 30 (2020): R921–R925, https://doi.org/10.1016/j.cub.2020.06.081.

27. D. Akhoundova and M. A. Rubin, "Clinical Application of Advanced Multi-Omics Tumor Profiling: Shaping Precision Oncology of the Future," *Cancer Cell* 40 (2022): 920–938, https://doi.org/10.1016/j.ccell.2022.08.011.

28. Y. Liu, M. Chen, L. Zhang, et al., "Comparisons in Microglial Responses to Ischemic–Hypoxic Brain Injury in Neonatal and Adult Mice Analyzed by Transcriptome Integration and Deconvolution Technologies," *Advanced Technology in Neuroscience* 2 (2025): 161–172, https://doi.org/10.4103/ATN.ATN-D-25-00004.

29. X. Li and C.-Y. Wang, "From Bulk, Single-Cell to Spatial RNA Sequencing," *International Journal of Oral Science* 13 (2021): 36, https://doi.org/10.1038/s41368-021-00146-0.

30. K. Xia, T. Wang, Z. Chen, et al., "Hepatocellular SETDB1 Regulates Hepatic Ischemia-Reperfusion Injury Through Targeting Lysine Methylation of ASK1 Signal," *Research* 6 (2023): 0256, https://doi.org/10.34133/research.0256.

31. Y. Lei, R. Tang, J. Xu, et al., "Applications of Single-Cell Sequencing in Cancer Research: Progress and Perspectives," *Journal of Hematology & Oncology* 14 (2021): 91, https://doi.org/10.1186/s13045-021-01105-2.

32. Q. Guo, Q. Wang, J. Chen, et al., "Dihydroartemisinin Regulated the MMP-Mediated Cellular Microenvironment to Alleviate Rheumatoid Arthritis," *Research* 7 (2024): 0459, https://doi.org/10.34133/research.0459.

33. J. Chen, L. Larsson, A. Swarbrick, and J. Lundeberg, "Spatial Landscapes of Cancers: Insights and Opportunities," *Nature Reviews Clinical Oncology* 21 (2024): 660–674, https://doi.org/10.1038/s41571-024-00926-7.

34. D. He, Z. Yang, T. Zhang, et al., "Multi-Omics and Machine Learning-Driven CD8+ T Cell Heterogeneity Score for Head and Neck Squamous Cell Carcinoma," *Molecular Therapy: Nucleic Acids* 36 (2025): 102413, https://doi.org/10.1016/j.omtn.2024.102413.

35. J. G. Greener, S. M. Kandathil, L. Moffat, and D. T. Jones, "A Guide to Machine Learning for Biologists," *Nature Reviews. Molecular Cell Biology* 23 (2022): 40–55, https://doi.org/10.1038/s41580-021-00407-0.

36. A. R. Zhao, R. Yuan, V. L. Kouznetsova, and I. F. Tsigelny, "Application of Machine Learning Technology and miRNA Biomarkers: A Novel Approach for Epilepsy Diagnosis," *Advanced Technology in Neuroscience* 2 (2025): 145–151, https://doi.org/10.4103/ATN.ATN-D-25-00017.

37. I. H. Sarker, "Machine Learning: Algorithms, Real-World Applications and Research Directions," *SN Computer Science* 2 (2021): 160, https://doi.org/10.1007/s42979-021-00592-x.

38. Y. Gao, J. Mu, K. Liu, and M. Wang, "Integrating Molecular Fingerprints With Machine Learning for Accurate Neurotoxicity Prediction: An Observational Study," *Advanced Technology in Neuroscience* 2 (2025): 109, https://doi.org/10.4103/ATN.ATN-D-24-00034.

39. Z. Liu, L. Liu, S. Weng, et al., "Machine Learning-Based Integration Develops an Immune-Derived lncRNA Signature for Improving Outcomes in Colorectal Cancer," *Nature Communications* 13 (2022): 816, https://doi.org/10.1038/s41467-022-28421-6.

40. M. J. Abraham, T. Murtola, R. Schulz, et al., "GROMACS: High Performance Molecular Simulations Through Multi-Level Parallelism From Laptops to Supercomputers," *SoftwareX* 1-2 (2015): 19–25, https://doi.org/10.1016/j.softx.2015.06.001.

41. D. Van Der Spoel, E. Lindahl, B. Hess, G. Groenhof, A. E. Mark, and H. J. C. Berendsen, "GROMACS: Fast, Flexible, and Free," *Journal of Computational Chemistry* 26 (2005): 1701–1718, https://doi.org/10.1002/jcc.20291.

42. C. Liu, M. Sun, Y. Wang, et al., "Ultraviolet Radiant Energy-Dependent Functionalization Regulates Cellular Behavior on Titanium

Dioxide Nanodots," *ACS Applied Materials & Interfaces* 12 (2020): 31793–31803, https://doi.org/10.1021/acsami.0c07761.

43. W. Guo, D. Wang, S. Wang, Y. Shan, C. Liu, and J. Gu, "scCancer: A Package for Automated Processing of Single-Cell RNA-Seq Data in Cancer," *Briefings in Bioinformatics* 22 (2021): bbaa127, https://doi.org/10.1093/bib/bbaa127.

44. A. P. Patel, I. Tirosh, J. J. Trombetta, et al., "Single-Cell RNA-Seq Highlights Intratumoral Heterogeneity in Primary Glioblastoma," *Science* 344 (2014): 1396–1401, https://doi.org/10.1126/science.1254257.

45. X. Pan, X. Li, L. Dong, et al., "Tumour Vasculature at Single-Cell Resolution," *Nature* 632 (2024): 429–436, https://doi.org/10.1038/s41586-024-07698-1.

46. A. M. Raghubar, M. J. Roberts, S. Wood, H. G. Healy, A. J. Kassianos, and A. J. Mallett, "Cellular Milieu in Clear Cell Renal Cell Carcinoma," *Frontiers in Oncology* 12 (2022): 943583, https://doi.org/10.3389/fonc.2022.943583.

47. H. Sung, J. Ferlay, R. L. Siegel, et al., "Global Cancer Statistics 2020: GLOBOCAN Estimates of Incidence and Mortality Worldwide for 36 Cancers in 185 Countries," *CA: A Cancer Journal for Clinicians* 71 (2021): 209–249, https://doi.org/10.3322/caac.21660.

48. C. S. A. Davan-Wetton, E. Pessolano, M. Perretti, and T. Montero-Melendez, "Senescence Under Appraisal: Hopes and Challenges Revisited," *Cellular and Molecular Life Sciences* 78 (2021): 3333–3354, https://doi.org/10.1007/s00018-020-03746-x.

49. D. Muñoz-Espín and M. Serrano, "Cellular Senescence: From Physiology to Pathology," *Nature Reviews. Molecular Cell Biology* 15 (2014): 482–496, https://doi.org/10.1038/nrm3823.

50. S. Chaib, T. Tchkonia, and J. L. Kirkland, "Cellular Senescence and Senolytics: The Path to the Clinic," *Nature Medicine* 28 (2022): 1556–1568, https://doi.org/10.1038/s41591-022-01923-y.

51. Y. Yan, A. Luo, S. Liu, et al., "METTL3-Mediated LINC00475 Alternative Splicing Promotes Glioma Progression by Inducing Mitochondrial Fission," *Research* 7 (2024): 0324, https://doi.org/10.34133/research.0324.

52. Z. Chen, J. Shi, and L. Li, "Application of Single-Cell Sequencing Technology and Its Clinical Implications in Parkinson's Disease and Alzheimer's Disease: A Narrative Review," *Advanced Technology in Neuroscience* 2 (2025): 9–15, https://doi.org/10.4103/ATN.ATN-D-24-00015.

53. D. L. Jardim, A. Goodman, D. de Melo Gagliato, and R. Kurzrock, "The Challenges of Tumor Mutational Burden as an Immunotherapy Biomarker," *Cancer Cell* 39 (2021): 154–173, https://doi.org/10.1016/j.ccell.2020.10.001.

54. R. N. Kaplan, R. D. Riba, S. Zacharoulis, et al., "VEGFR1-Positive Haematopoietic Bone Marrow Progenitors Initiate the Pre-Metastatic Niche," *Nature* 438 (2005): 820–827, https://doi.org/10.1038/nature04186.

55. H. L. Goel and A. M. Mercurio, "VEGF Targets the Tumour Cell," *Nature Reviews Cancer* 13 (2013): 871–882, https://doi.org/10.1038/nrc3627.

56. C. Ceci, M. G. Atzori, P. M. Lacal, and G. Graziani, "Role of VEGFs/VEGFR-1 Signaling and Its Inhibition in Modulating Tumor Invasion: Experimental Evidence in Different Metastatic Cancer Models," *International Journal of Molecular Sciences* 21 (2020): 1388, https://doi.org/10.3390/ijms21041388.

57. M. Verma, Y. Asakura, X. Wang, et al., "Endothelial Cell Signature in Muscle Stem Cells Validated by VEGFA-FLT1-AKT1 Axis Promoting Survival of Muscle Stem Cell," *eLife* 13 (2024): e73592, https://doi.org/10.7554/eLife.73592.

58. X. Lu, C. Zhang, L. Zhu, et al., "TBL2 Promotes Tumorigenesis via PRMT5/WDR77-Mediated AKT Activation in Breast Cancer," *Advanced Science (Weinheim, Baden-Wurttemberg, Germany)* 11 (2024): e2400160, https://doi.org/10.1002/advs.202400160.

59. J. Ye, S. Wu, Q. Quan, et al., "Fibroblast Growth Factor Receptor 4 Promotes Triple-Negative Breast Cancer Progression via Regulating Fatty Acid Metabolism Through the AKT/RYR2 Signaling," *Cancer Medicine* 13 (2024): e70439, https://doi.org/10.1002/cam4.70439.

60. Y. Watanabe, S. W. Lee, M. Detmar, I. Ajioka, and H. F. Dvorak, "Vascular Permeability Factor/Vascular Endothelial Growth Factor (VPF/VEGF) Delays and Induces Escape From Senescence in Human Dermal Microvascular Endothelial Cells," *Oncogene* 14 (1997): 2025–2032, https://doi.org/10.1038/sj.onc.1201033.

61. J.-i. Nishi, T. Minamino, H. Miyauchi, et al., "Vascular Endothelial Growth Factor Receptor-1 Regulates Postnatal Angiogenesis Through Inhibition of the Excessive Activation of Akt," *Circulation Research* 103 (2008): 261–268, https://doi.org/10.1161/CIRCRESAHA.108.174128.

62. J. E. Skeen, P. T. Bhaskar, C.-C. Chen, et al., "Akt Deficiency Impairs Normal Cell Proliferation and Suppresses Oncogenesis in a p53-Independent and mTORC1-Dependent Manner," *Cancer Cell* 10 (2006): 269–280, https://doi.org/10.1016/j.ccr.2006.08.022.

63. S. Pandurangan, D. Kuppuram, R. Arunkumar, and N. Nagarajan, "Targeting Cellular Senescence: Therapeutic Advances in Senolytic and Senomorphic Interventions for Age-Related Pathologies," *Curr Top Med Chem* (2026), accessed March 14, https://www.eurekaselect.com/article/153407.

64. M. Ogrodnik, J. C. Acosta, P. D. Adams, et al., "Guidelines for Minimal Information on Cellular Senescence Experimentation In Vivo," *Cell* 187 (2024): 4150–4175, https://doi.org/10.1016/j.cell.2024.05.059.

65. L. Lin, J. Zhong, F. Jiang, et al., "A Single-Cell Time-Series Atlas of Endothelial Cell Embryonic Development," *Cell* 189 (2026): 1573–1590.e24, https://doi.org/10.1016/j.cell.2026.01.002.

66. Z. Lu, P. Fang, S. Li, et al., "Lactylation of Histone H3k18 and Egr1 Promotes Endothelial Glycocalyx Degradation in Sepsis-Induced Acute Lung Injury," *Advanced Science* 12 (2025): 2407064, https://doi.org/10.1002/advs.202407064.

67. Q. Zeng, M. Mousa, A. S. Nadukkandy, et al., "Understanding Tumour Endothelial Cell Heterogeneity and Function From Single-Cell Omics," *Nature Reviews Cancer* 23 (2023): 544–564, https://doi.org/10.1038/s41568-023-00591-5.

68. L. Jakobsson, C. A. Franco, K. Bentley, et al., "Endothelial Cells Dynamically Compete for the Tip Cell Position During Angiogenic Sprouting," *Nature Cell Biology* 12 (2010): 943–953, https://doi.org/10.1038/ncb2103.

69. Y. Zhang, S. P. Narayanan, R. Mannan, et al., "Single-Cell Analyses of Renal Cell Cancers Reveal Insights Into Tumor Microenvironment, Cell of Origin, and Therapy Response," *Proceedings of the National Academy of Sciences* 118 (2021): e2103240118, https://doi.org/10.1073/pnas.2103240118.

70. M. D. Young, T. J. Mitchell, F. A. Vieira Braga, et al., "Single-Cell Transcriptomes From Human Kidneys Reveal the Cellular Identity of Renal Tumors," *Science* 361 (2018): 594–599, https://doi.org/10.1126/science.aat1699.

71. G. S. Gulati, S. S. Sikandar, D. J. Wesche, et al., "Single-Cell Transcriptional Diversity is a Hallmark of Developmental Potential," *Science* 367, no. 6476 (2020): 405–411.

72. A. H. Banday, "Harnessing the Immune System and Developing Targeted Vaccines: Overall Strategies of Leveraging the Body's Natural Defense Mechanisms to Enhance Cancer Treatment," *Regenerative Medicine Reports* 2 (2025): 185–192, https://doi.org/10.4103/REGENMED.REGENMED-D-25-00011.

73. H. Jin, L. Wang, and R. Bernards, "Rational Combinations of Targeted Cancer Therapies: Background, Advances and Challenges,"

Nature Reviews Drug Discovery 22 (2023): 213–234, https://doi.org/10.1038/s41573-022-00615-z.

74. F.-M. Fan, J. S. Fleishman, J. Chen, Z.-S. Chen, and H.-H. Dong, "New Insights Into the Mechanism of Resistance to Lenvatinib and Strategies for Lenvatinib Sensitization in Hepatocellular Carcinoma," *Drug Discovery Today* 29 (2024): 104069, https://doi.org/10.1016/j.drudis.2024.104069.

75. J.-Y. Blay, F. Duffaud, S. George, R. G. Maki, and N. Penel, "Regorafenib for the Treatment of Sarcoma," *Current Treatment Options in Oncology* 23 (2022): 1477–1502, https://doi.org/10.1007/s11864-022-00990-0.

76. N. Nano, F. Ugwu, T. V. Seraphim, et al., "Sorafenib as an Inhibitor of RUVBL2," *Biomolecules* 10 (2020): 605, https://doi.org/10.3390/biom10040605.

77. Y. Man, Y. Han, M. Sarbajit, and Z. Olivia, "Incidence of Hypertension and Proteinuria in Patients Treated With Bevacizumab Versus Bevacizumab Biosimilar," *Journal of Clinical Oncology* 39 (2021): 83, https://doi.org/10.1200/JCO.2021.39.3_suppl.83.

78. C. Fernandez-Teruel, M. Cullberg, C. Eberlein, S. T. Barry, and D. Zhou, "Population Pharmacokinetics of Capivasertib in Patients With Advanced or Metastatic Solid Tumours," *Clinical Pharmacokinetics* 63 (2024): 1191–1204, https://doi.org/10.1007/s40262-024-01407-x.

79. V. P. Kale, H. Hasan, C. Robert, et al., "Old Drugs, New Uses: Drug Repurposing in Hematological Malignancies," *Seminars in Cancer Biology* 68 (2021): 242–248, https://doi.org/10.1016/j.semcancer.2020.03.005.

Supporting Information

Additional supporting information can be found online in the Supporting Information section. **Figure S1:** Identification of cell clusters with diverse annotations revealing high cellular heterogeneity in ccRCC based on single-cell analysis. (A) The variance diagram showing the variation of gene expression in all cells, where the red dots represent highly variable genes and the black dots represent non-variable genes. (B) PCA and harmony analysis showing a clear separation of all cells. (C) Harmony analysis identifying the top 20 PCs at $p < 0.05$ in all cells. (D) Classification of cell clusters in all cells. (E) Identification of core cells after quality control of scRNA-seq in normal tissue cells. (F) Variance diagram showing the variation of gene expression in normal tissue cells. (G) PCA and harmony analysis showing a clear separation of normal tissue cells. (H) Harmony analysis identifying the top 50 PCs at $p < 0.05$ in normal tissue cells. (I) Classification of cell clusters in normal tissue cells. (J) Identification of core cells after quality control of scRNA-seq in tumor cells. (K) The variance diagram showing the variation of gene expression in tumor cells. (L) PCA and harmony analysis showing a clear separation of tumor cells. (M) Harmony analysis identifying the top 50 PCs at $p < 0.05$ in tumor cells. (N) Classification of cell clusters in tumor cells. (O–R) GO and KEGG analysis showing the pathways affected by marker genes in tumor. **Figure S2:** WGCNA analysis and cellular senescence subtypes. (A) Consensus heatmap defining the two clusters ($k = 2$). (B) Relative change in area under the CDF curve from k 2–9. (C) Consensus CDF in consistent clustering ($k = 2$–9). (D) Tracking plot of the ccRCC samples ($k = 2$–9). (E-F) Analysis of the scale-free index for various soft-threshold powers (β). (G) Clustering of module eigengenes. MEDissThres = 0.5. **Figure S3:** Construction and validation of the cellular senescence-related signature. (A) Survival curve, survival status, and heatmaps showing the expression of signature genes of patients with ccRCC in TCGA-all subset. (B) K–M survival analysis showing a significant survival difference between low- and high-risk ccRCC in the TCGA-all subset. (C) ROC analysis showing the stable prediction ability of the cellular senescence-related signature in TCGA-all subset. (D) PCA showing the clear separation of low- and high-risk ccRCC of the patients in TCGA-all subset. (E–H) Similar to D–G, but the patients with ccRCC were in TCGA-test subset. (I–L) Similar to D–G, but the patients with ccRCC were in TCGA-training subset. (M) GSEA identifying the top 10 gene sets in high-risk ccRCC. (N) GSEA identifying the top six gene sets in low-risk group. (O) Overall description of the TCGA-KIRC patient mutation landscape. **Figure S4:** Clinical character analysis and nomogram. (A–F) Correlation analysis of risk scores with clinical characteristics showing relationship between age, sex, M stage, N stage, T stage, and tumor stage with the analysis model. (G) Univariate Cox analysis and multifactorial Cox analysis of risk scores and clinical characteristics in the training subset. (H) Univariate Cox analysis and multifactorial Cox analysis in the test subset. (I) Heatmap of clinical features and senescent gene expression levels of TCGA subset. (J) Construction of the nomogram model. (K) The calibration curve of the nomogram. (L) ROC curves showing the predictive effect of the models. **Figure S5:** K–M survival analysis presenting the significance of prognosis between low- and high-risk ccRCC in subgroups of (A, B) female, male, (C, D) age ≥ 65, age < 65, (E, F) M0, M1, (G, H) clinical stage I–II, clinical stage III–IV, (I–L) clinical stage I, clinical stage II, clinical stage III, clinical stage IV, (M–P) T1–2, T3–4, T1, T2, and T3. **Figure S6:** (A) Elastic net algorithm for the importance of the five genes. (B) Naive Bayes algorithm for the importance of the five genes. (C) StepLDA algorithm for the importance of the five genes. (D) SVM algorithm for the importance of the five genes. **Figure S7:** Enrichment analysis of FLT1. (A) The immune infiltration status of patients with high and low expression of FLT1. (B) Correlation analysis of FLT1 and immune cells. (C) GSEA identifying the enriched functions of FLT1. **Figure S8:** Expression of FOXM1, GADD45G, GNMT, and NDRG1. (A) The differential expression of five genes between normal and tumor tissues. (B) Expression of FOXM1 in different cell clusters. (C) The immune infiltration status of patients with high and low expression of FOXM1. (D) Correlation analysis of FOXM1 and immune cells. (E) Expression of GADD45G in different cell clusters. (F) The immune infiltration status of patients with high and low expression of GADD45G. (G) Correlation analysis of GADD45G and immune cells. (H) Expression of GNMT in different cell clusters. (I) The immune infiltration status of patients with high and low expression of GNMT. (J) Correlation analysis of GNMT and immune cells. (K) Expression of NDRG1 in different cell clusters. (L) The immune infiltration status of patients with high and low expression of NDRG1. (M) Correlation analysis of NDRG1 and immune cells. **Figure S9:** Machine learning. (A) Elastic net algorithm for the importance of PGF, VEGFB, and VEGFA. (B) SVM algorithm for the importance of NFATC2, and AKT1. (B) Naive Bayes algorithm for the importance of NFATC2, and AKT1. (B) StepLDA algorithm for the importance of NFATC2, and AKT1. **Figure S10:** Correlation of the FLT1-centered regulatory network and cellular senescence-related genes. (A) ROC analysis of the FLT1-centered regulatory network. (B–E) Correlation of AKT1 and cellular senescence-related genes. (F–K) Correlation of FLT1 and cellular senescence-related genes. (L–P) Correlation of VEGFA and cellular senescence-related genes. **Figure S11:** Expression of VEGFB and PGF. (A) The relative expression levels of VEGFB in ccRCC clinical samples. $n = 5$ per group. (B) The relative expression levels of PGF in ccRCC clinical samples. $n = 5$ per group. **Figure S12:** Single-cell analysis of endothelial and epithelial cell subsets. (A) The CNV quantities of cells in different clusters. (B) Relative contribution of each ligand-receptor pair to the main signaling pathway between each cell cluster. (C) Relative contribution of each ligand-receptor pair in the VEGF signaling pathway between each cell cluster. **Figure S13:** Single-cell analysis of ccRCC in mice. (A) The variance diagram showing the variation of gene expression in all cells, where the red dots represent highly variable genes and the black dots represent non-variable genes. (B) PCA and harmony analysis showing a clear separation of all cells. (C) Elbow Plot. (D) Different sample in tSNE. (E) Classification of cell clusters.